

ALES: a multi-mission adaptive sub-waveform retracker for coastal and open ocean altimetry

Marcello Passaro^a, Paolo Cipollini^b, Stefano Vignudelli^c, Graham Quartly^d, Helen Snaith^e

^a*GSNOCS, University of Southampton, Waterfront Campus European Way, SO14 3ZH, Southampton, UK. Contacts: marcello.passaro@noc.soton.ac.uk, 00442380596488*

^b*National Oceanography Centre, Southampton*

^c*Consiglio Nazionale delle Ricerche, Istituto di Biofisica, Pisa*

^d*Plymouth Marine Laboratory*

^e*British Oceanographic Data Centre, Southampton*

Abstract

Satellite altimetry has revolutionized our understanding of ocean dynamics thanks to frequent sampling and global coverage. Nevertheless, coastal data have been flagged as unreliable due to land and calm water interference in the altimeter and radiometer footprint and uncertainty in the modelling of high-frequency tidal and atmospheric forcing.

Our study addresses the first issue, i.e. altimeter footprint contamination, via re-tracking, presenting ALES, the Adaptive Leading Edge Subwaveform retracker. ALES is potentially applicable to all the pulse-limited altimetry missions and its aim is to retrack both open ocean and coastal data with the same accuracy using just one algorithm.

ALES selects part of each returned echo and models it with a classic "open ocean" Brown functional form, by means of least square estimation whose convergence is found through the Nelder-Mead nonlinear optimization technique. By avoiding echoes from bright targets along the trailing edge, it is capable of retrieving more coastal waveforms than the standard processing. By adapting the width of the estimation window according to the significant wave height, it aims at maintaining the accuracy of the standard processing in both the open ocean and the coastal strip.

This innovative retracker is validated against tide gauges in the Adriatic Sea and in the Greater Agulhas System for three different missions: Envisat, Jason-1 and Jason-2. Considerations of noise and biases provide a further verification of the strategy. The results show that ALES is able to provide more reliable 20-Hz data for all three missions in areas where even 1-Hz averages are flagged as unreliable in standard products. Application of the ALES retracker led to roughly a half of the analysed tracks showing a

marked improvement in correlation with the tide gauge records, with the rms difference being reduced by a factor of 1.5 for Jason-1 and Jason-2 and over 4 for Envisat in the Adriatic Sea (at the closest point to the tide gauge).

Keywords: Coastal Altimetry, retracking, subwaveform retracker, validation, tide gauge, satellite altimetry;

1. Introduction

1 Satellite altimetry, one of the most successful applications of remote sensing at the
2 service of earth science and climate studies, is based on a simple radar principle. The
3 fundamentals of satellite altimetry are comprehensively described in Chelton et al. (2001).
4 A short pulse of radiation with known power is transmitted from a satellite towards the
5 sea. The pulse interacts with the rough sea surface and part of the incident radiation
6 within the altimetric footprint reflects back to the radar altimeter, which records the
7 returned echo of the pulse. The power of the signal as received by the satellite is registered
8 in a time series called a "waveform", sampled with a two-way travel time resolution of
9 3.125 ns; each resolution cell is known as a "gate". The acquisition depends on the
10 functioning of the on-board tracker, which adjusts the altimeter observation window in
11 time in order to keep the reflected signal coming from the Earth within the window. The
12 output of the on-board tracker is the "Tracker Range", which is a first estimation of the
13 distance between the satellite and the sea surface.

14 Each individual echo is strongly perturbed by Rayleigh noise (speckle) coming from the
15 incoherent addition of signals from reflecting facets inside the satellite footprint (Quartly
16 et al., 2001). Assuming that noise on consecutive waveforms is uncorrelated (which sets
17 an upper boundary on the useful pulse repetition frequency of the altimeter (Walsh,
18 1982)), it can be reduced by averaging a number of waveforms prior to transmission
19 (downlink) to the ground. Typical downlinked "high-rate" waveforms at ~ 20 Hz are an
20 average of 100 consecutive samples at ~ 2 kHz (Quartly et al., 2001). In order to retrieve
21 geophysical information from these waveforms, a processing step called "retracking" has
22 to be performed on the ground (Chelton et al., 2001). The retracking process consists
23 of fitting a model response to the real waveform. Over the open ocean, most waveforms
24 are well described by the Brown-Hayne mathematical model (Brown, 1977; Hayne, 1980),
25 which we recall in section 3 and which is the standard model used for retracking waveforms

26 over ocean surfaces.

27 Waveforms that conform to the Brown-Hayne model present a fast-rising leading edge
28 and a slowly-decaying trailing edge. Figure 1 shows the characteristics of an idealized
29 open ocean waveform without noise, in order to define the parameters of interest for the
30 retracking. The mid-point of the leading edge is chosen as an estimate of the distance
31 between the satellite and the sea surface (range), since it is related to the sea surface mean
32 position at nadir. The leading edge is therefore particularly important for the retracking,
33 since it contains the parameters that a retracker usually estimates: the position of the
34 mid-point of the leading edge with respect to the fixed nominal tracking point determined
35 by the on-board tracker (Epoch τ); the rise time of the leading edge, which is related to
36 the significant wave height (SWH); the amplitude of the received signal, from which the
37 backscatter coefficient σ^0 is derived and then related to the wind speed. The retracked
38 range is computed by adding the Epoch to the Tracker Range.

39 The residual noise of real waveforms, particularly evident along the trailing edge, can
40 influence the correct retrieval of the parameters of interest in the retracking process, since
41 the waveforms deviate from the theoretical open ocean shape. This is known to happen
42 in particular in the last 10 km from the coastline: at this distance, both coastal waters
43 and raised land can give returns within the altimeter's range window. In these cases, the
44 waveform shape changes from that expected for a homogeneous surface. Several studies
45 in recent years have classified coastal waveforms (Deng et al., 2002; Berry et al., 2010;
46 Andersen et al., 2010). Two of the predominant coastal waveform classes are quasi-
47 specular and multi-peak echoes (Idris & Deng, 2012). They are both connected with the
48 presence of highly reflective targets (bright targets) whose signatures are seen tracing an
49 hyperbola in consecutive waveforms (Gommenginger et al., 2011).

50 The physical features causing bright targets are still subject to debate. Tournadre
51 (2007) states that signals coming from small targets like ships are only detected in the
52 first gates before the leading edge, while land features such as islands can influence the
53 entire waveform due to their high backscatter coefficient. In the same study, the fact
54 that coastal bright targets are not present in every cycle is attributed to exposure of tidal
55 flats by the tidal cycle. Recently, the same author has led a study demonstrating the
56 detection of icebergs in the open ocean based on the presence of bright targets in the
57 gates preceding the leading edge (Tournadre et al., 2012). Gomez-Enri et al. (2010) and

58 Scozzari et al. (2012) have investigated the bright targets over a coastal area near the
59 island of Pianosa. They both concluded that the presence of patches of high reflectance
60 is not a constant event and that they are most likely related to sea state and can be
61 generated by unbroken wave crests and patches of calm water.

62 Figure 2 shows six along-track radargrams (stacks of consecutive hi-rate waveforms,
63 one for each column) from Envisat track 416 flying over the northern end of the Adriatic
64 Sea (map in figure 3). Land is shaded in grey. The colorbar codes the power of each gate
65 for every waveform. Brighter features in the speckle noise along the trailing edge are seen
66 progressing from later gates towards the leading edge and back, along hyperbolic paths
67 as expected from simple geometrical arguments (Gomez-Enri et al., 2010).

68 Using geometry considerations described in Quartly (1998) and assuming that the
69 actual tracking point is not significantly different from its nominal position, it is possible
70 to compute the distance of the last gate of the waveform from the nominal tracking
71 point, i.e. the radius of the satellite footprint at the end of the trailing edge, which is
72 7.3 km for Envisat and 8.3 km for Jason for calm seas. Depending on the elevation, land
73 returns could still appear in the trailing edge, even if the surface is located outside the
74 expected footprint, because their location could be equidistant with the ocean surface
75 near nadir. Nevertheless, this would produce a more predictable hyperbolic feature than
76 what is shown in the radargrams, where bright targets are not seen constantly at every
77 cycle and their location and extent varies. It is therefore evident that the perturbations
78 cannot be exclusively attributed to land in the satellite footprint.

79 Regardless of their origin, these features degrade the estimation of geophysical pa-
80 rameters based on Brown-Hayne retracking. To avoid this problem, different dedicated
81 coastal retracking solutions have been suggested and tested in recent years. The latest
82 strategies involve one or a combination of the following methods:

- 83 • the classification of the waveforms depending on their shape (Deng & Featherstone,
84 2006; Berry et al., 2010; Andersen et al., 2010; Yang et al., 2012)
- 85 • the use of empirical parameters and/or threshold values to model the waveform
86 (Deng & Featherstone, 2006; Hwang et al., 2006; Bao et al., 2009; Lee et al., 2010)
- 87 • the adaptation of a different functional form for every kind of characteristic shape
88 that the waveforms can assume (Berry et al., 1997; Andersen et al., 2010)

- 89 • the simultaneous processing of multiple waveforms to detect the bright targets prior
90 to retracking (Gomez-Enri et al., 2010; Quartly, 2010)
- 91 • the addition of peaks to the Brown-Hayne functional form to model the presence
92 of bright targets (Halimi et al., 2012)
- 93 • the retracking of subwaveforms, i.e. portion of waveforms not affected by the bright
94 targets (Mercier et al., 2009; Guo et al., 2010; Yang et al., 2011, 2012; Idris & Deng,
95 2012)

96 Most of these attempts have been successful in demonstrating that meaningful geo-
97 physical estimates can be retrieved from data records which were previously disregarded.
98 However there are a number of still unresolved issues. The use of empirical and threshold
99 retrackers lacks a physical description of the functional form; moreover the choice of pa-
100 rameters might vary in different coastal conditions. The addition of further parameters
101 (peaks) to the model can improve the overall fitting of the waveform without necessarily
102 resulting in a better fitting of the three important parameters (τ , SWH, σ^0), and also
103 introduces additional complications in terms of numerical convergence of the estimation.
104 The use of different retrackers depending on conditions and the switching from one to
105 another, requires an accurate quantification of biases amongst them, to avoid "jumps" in
106 the retrieved parameters. Even the simple distinction between open and coastal ocean
107 to apply different retracking strategies raises questions about where the boundary should
108 be set, and what are the consequences of introducing such a discontinuity.

109 In this study we present the Adaptive Leading Edge Sub-waveform (ALES) retracker,
110 which will overcome the above difficulties as it can be applied both over open and coastal
111 ocean without discontinuity. ALES represents an evolution of the family of the sub-
112 waveform retrackers, in that it adapts the width of the sub-waveform according to the
113 SWH. ALES is designed in order to maintain the same degree of precision both in open
114 ocean and along the coasts. As we will demonstrate, ALES performs only marginally
115 worse than the Brown-Hayne retracker over waveforms that comply with the Brown-
116 Hayne model, but it outperforms the Brown-Hayne retracker for the vast majority of
117 open ocean waveforms affected by bright targets, as well as in coastal waters. One of
118 ALES strengths lies in the fact that it does not involve any change in the retracking
119 method, hereby avoiding any source of potential internal bias. It succeeds in retracking

120 waveforms where the trailing edge is contaminated, but a distinct leading edge is still
121 observable.

122 The rationale for ALES comes from recent studies on leading edge retracers, but
123 also from concepts deeply embedded in the design of the first altimetric missions. The
124 tracker system designs of the SEASAT, GEOSAT and TOPEX missions, while using the
125 rising leading edge as the basis of precise height measurement, estimated the height error
126 (degradation of measurement precision with increasing wave height) using a number of
127 gates increasing with increasing wave height (Marth et al., 1993). The variation in width
128 of the fitting window with SWH makes ALES widely applicable to different environmental
129 conditions as we demonstrate over two regions with very different sea state. Moreover
130 ALES is applicable to waveforms from different altimeters, as we show in this study with
131 data from Envisat, Jason-1 and Jason-2: to our knowledge this is the first time that
132 the same coastal-dedicated retracker has been applied and validated for three different
133 altimetry missions.

134 Section 2 presents the datasets that have been used in the study. Section 3 describes
135 the mathematical details and the functioning of ALES. The sea level estimation from
136 ALES is then validated for the three altimetric missions in section 4, where the results
137 are presented and discussed. Section 5 draws the conclusions and the outlook for future
138 research enabled by ALES.

139 **2. Dataset**

140 Two areas of study (shown in 3) were selected to verify and validate ALES: the Gulf
141 of Trieste, in the North-West Adriatic Sea, and Mossel Bay, along the Indian Ocean coast
142 of South Africa. The areas are representative of two different morphological and oceanic
143 conditions.

144 The Gulf of Trieste is a small shallow bay with average depth: 17 m, maximum depth:
145 25 m and width: 20 km. The maximum tidal amplitude is 81 cm (Querin et al., 2006).
146 The cyclonic gyre (anticlockwise) that characterises the main circulation is induced by
147 currents flowing northwards along the Istrian coast and is modulated daily by the local
148 wind field (Querin et al., 2006). The rest of the Northern Adriatic basin is also a shallow
149 sea, less than 100 m deep. It is characterised by a weak cyclonic circulation that reaches
150 peaks of 25 cm/s along the Italian coast of its western boundary (Poulain, 2001).

151 Wind strength and direction is particularly important because of its influence on the
152 sea surface roughness. The most important wind in the Gulf of Trieste in terms of fre-
153 quency and intensity is called the Bora (from East-North-East), with further contributions
154 to atmospheric circulation from Scirocco (direction South-East to South-South-West) and
155 breezes from land and sea. The Bora is a strong katabatic wind which can reach speeds
156 of over 10 m/s, especially during autumn/winter and has an annual mean velocity of 6
157 m/s (compared to 2.1 m/s for the other winds in the region) (Stravisi, 1977).

158 Mossel Bay is a much more open 25 km wide gulf, affected by the large circulation
159 features of the South African coast. From the coast, the Agulhas Bank extends for roughly
160 200 km with depths that do not exceed 200 m and near-surface currents in the range of
161 0-0.5 m/s. Then the continental slope is found, where the prevailing westward warm
162 Agulhas Current reaches velocities of 2.50 m/s and the depth rapidly reaches over 4000
163 m (Boyd & Shillington, 1994). The amplitude of spring tide reaches 2.40 m (South African
164 Navy, 2007). Wind forcing is particularly important along the coast and influences the
165 surface currents of the bank. Easterly winds prevail in the summer, causing coastal
166 upwelling, while westerly winds predominate in winter (Schumann, 1992).

167 In these two locations, waveforms from 5 tracks from 3 different altimetry satellites
168 were retracked with ALES. The waveforms are provided as part of the SGDR (Sen-
169 sor Geophysical Data Record) product for each mission, which also includes the level 2
170 geophysical estimates of height, SWH and wind based on the Brown-Hayne retracker, to-
171 gether with atmospheric and geophysical corrections to be applied to the data. They are
172 distributed at 18 Hz rate for Envisat and 20 Hz rate for Jason-1 and Jason-2, representing
173 a measurement every 300-350 metres.

174 As a reference and comparison, data from CTOH (Centre for Topographic studies
175 of the Ocean and Hydrosphere, <http://ctoh.legos.obs-mip.fr/altimetry>) have been down-
176 loaded. In particular, the 1-Hz (a measurement approximately every 7 km) along track
177 altimetry output from X-TRACK processor is used. At the time of this research, data
178 were available for all the tracks except for Envisat pass 687. Data were developed, vali-
179 dated and distributed by the CTOH/LEGOS, France. The X-TRACK processor does not
180 retrack the waveforms; it is a post-processing technique aimed at improving quality and
181 quantity of coastal altimetry measurements through improved tidal and atmosphere forc-
182 ing correction, data editing and filtering. A detailed description can be found in Roblou

183 et al. (2007) and Roblou et al. (2011). X-TRACK data are widely used and applications
184 already include the Mediterranean Sea (Birol et al., 2010; Bouffard et al., 2011; García
185 et al., 2012), the Spanish coast (Le Hénaff et al., 2011; Dussurget et al., 2011; Herbert
186 et al., 2011), the West Florida Shelf (Liu et al., 2012), Drake Passage (Ferrari et al., 2013)
187 and the Solomon Sea (Melet et al., 2010).

188 To create a time series, data points along the satellite tracks have to be collinear:
189 it is necessary to have measurements at the same geographical location for each cycle.
190 Nominal tracks were therefore created for this study by taking as a reference the CTOH
191 1-Hz tracks, neglecting the across-track displacement of different passes along the same
192 track, which is normally less than 1 km. Each interval between consecutive 1-Hz data
193 points was divided in order to obtain 20 equidistant nominal locations, along which the
194 altimeter data from SGDR and ALES for each cycle were then linearly interpolated.

195 Two tide gauges were used for validation of ALES output. They are located at Trieste
196 (PSMSL Station ID 154, Latitude 45.647361° N, Longitude 13.758472° E) and Mossel Bay
197 (PSMSL Station ID 910, Latitude -34.178611° N, Longitude 22.135278° E).

198 The Trieste tide gauge belongs to the Italian national tide gauge network operated
199 by ISPRA (High Institute for Environmental Protection and Research). The station is
200 equipped with a gauge that records sea level referred to the zero level of the Italian
201 altimetric network. The Italian altimetric network, created by IGM (Istituto Geografico
202 Militare) is the vertical reference (datum) to which all heights are measured around Italy.
203 The zero of the Italian altimetric network is the mean sea level, measured in Genoa during
204 the years 1937-1946 (Gamboni, 1965). For the Trieste station, it was possible to refer the
205 sea level measurements to the WGS84 ellipsoid, since the Italian zero level at the tide
206 gauge is estimated to be 44.760 m above it (Stravisi & Purga, 2005; Becker et al., 2002).
207 The sampling frequency is adjusted to provide data every 10 minutes and/or hourly.

208 Hourly data for Mossel Bay are distributed by the GLOSS/CLIVAR (Global Sea Level
209 Observing System / Climate Variability and Predictability) fast sea level data service.
210 Since we have been unable to find sources referring those measurements to the ellipsoid,
211 they have been used for relative calibration only.

212 Figure 3 shows the area of study, including the satellite tracks and tide gauges lo-
213 cations. It is relevant to point out the flight direction of each satellite as it flies over
214 each region, since land-to-sea and sea-to-land transitions might influence the behaviour

215 of the on-board tracker in different ways. In the Adriatic, Envisat pass 416 (Env 416) is
216 a descending (North to South) track, as is Jason-2 pass 196 (J-2 196), while Jason-1 pass
217 161 in its interleaved orbit (J-1 161) is ascending (South to North). All three tracks cross
218 part of the Gulf of Trieste and fly over the Istrian peninsula. For J-1 161 and Env 416,
219 the stretch of land in Istria accounts for a few km along-track, while J-2 196 flies over
220 the full extent of the peninsula. J-2 196 is particularly challenging because it also flies
221 over Marano Lagoon (classified as inland water), which is less than 3 m deep, and then
222 crosses a 0.5 km wide sandbar before entering the Adriatic Sea (Ferrarin et al., 2009).

223 Of the two tracks we have used along the coast of South Africa, Envisat pass 687 (Env
224 687) is an ascending track, while Jason-2 pass 198 (J-2 198) is descending. J-2 198 flies
225 over the same bay where the tide gauge is located, while Env 687 passes over the other
226 side of Mossel Bay peninsula.

227 Table 1 summarises the characteristics of the dataset and in particular the number
228 of waveforms that were missing from the along-track data and the number of waveforms
229 for which no altimetry parameter estimation was available in the SGDR. The number of
230 missing waveforms is obtained by checking how many times there are no waveforms that
231 fall in the interval between each latitude-longitude point of the nominal tracks. Missing
232 waveforms are more frequent in the Jason missions due to failures of the on-board tracker,
233 an event that particularly occurs near the transition from land to sea (Brooks et al., 1998),
234 which explains why the loss is concentrated in the first 10 km from the coast for the two
235 descending tracks of Jason-2, with up to 70% of data missing for the latitude-longitude
236 points located closest to the coast.

237 The Envisat altimeter was designed to operate at different bandwidths over different
238 surfaces. The bandwidth preferred for the ocean was 320 MHz, in order to guarantee
239 the highest possible resolution. Nevertheless in the transition zone it can happen that
240 returned echoes are acquired using a different bandwidth. For Envisat data, only SGDR
241 output when operated at 320 MHz bandwidth are considered valid. ALES only retracks
242 these waveforms.

243 A detailed list of all the cycles reprocessed for each satellite track and the related time
244 interval is provided in table 2.

245 **3. Retracker**

246 *3.1. Functional form*

247 ALES adopts the Brown-Hayne theoretical ocean model (Brown, 1977; Hayne, 1980),
 248 the same as in use for the open-ocean retracker, which describes the average return power
 249 of a rough scattering surface (i.e. what we simply call *waveform*). The return power V_m
 250 is

$$V_m(t) = a_\xi P_u \frac{[1 + \operatorname{erf}(u)]}{2} \exp(-v) + T_n \quad (1)$$

251 where

$$a_\xi = \exp\left(\frac{-4 \sin^2 \xi}{\gamma}\right) \quad \gamma = \sin^2(\theta_0) \frac{1}{2 \cdot \ln(2)}$$

$$\operatorname{erf}(x) = 2 \frac{1}{\sqrt{\pi}} \int_0^x e^{-t^2} dt$$

$$u = \frac{t - \tau - c_\xi \sigma_c^2}{\sqrt{2} \sigma_c} \quad v = c_\xi \left(t - \tau - \frac{1}{2} c_\xi \sigma_c^2 \right)$$

$$c_\xi = b_\xi a \quad b_\xi = \cos(2\xi) - \frac{\sin^2(2\xi)}{\gamma} \quad a = \frac{4c}{\gamma h \left(1 + \frac{h}{R_e}\right)}$$

$$\sigma_c^2 = \sigma_p^2 + \sigma_s^2 \quad \sigma_s = \frac{SWH}{2c}$$

252 where c is the speed of light, h the satellite altitude, R_e the Earth radius, ξ the off-
 253 nadir mispointing angle, θ_0 the antenna beam width, τ the Epoch with respect to the
 254 nominal tracking reference point, σ_c the rise time of the leading edge (depending on a
 255 term σ_s linked to SWH and on the width of the radar point target response σ_p), P_u the
 256 amplitude of the signal and T_n the thermal noise level.

257 In practice, the model in equation 1 is a raised sigmoid $\frac{[1 + \operatorname{erf}(u)]}{2}$ describing the in-
 258 creasing power in the waveform leading edge and the subsequent plateau, multiplied by a

259 negative exponential which models the reduction of power in the waveform tail (decay),
260 plus thermal (additive) noise T_n . The amplitude of the signal P_u is attenuated by a term
261 a_ξ dependant on mispointing ξ . P_u can be converted into a measurement of the backscat-
262 ter coefficient σ^0 on the basis of the instrument calibration. Note that the significant
263 wave height SWH , in addition to affecting the rise time of the waveform, also has a
264 small effect on the sigmoid location (variable u) and on the waveform decay (variable v),
265 via the term $c_\xi \sigma_c^2$.

266 A complete physical description of the functional form can be found in Brown (1977)
267 and Gommenginger et al. (2011).

268 3.2. Estimator

269 The model in 3.1. is fitted to the real signal in order to estimate the parameters of
270 interest. Chelton et al. (2001) suggested the use of least squares rather than maximum
271 likelihood estimation (MLE), because the latter assigns too much weight to portions of
272 the waveform with low signal power, and is therefore unreliable due to unmodeled errors
273 in the waveform samples. For Envisat, Jason-1 and Jason-2 the optimal parameters are
274 found at each iteration by developing the total cost function in a Taylor series at first
275 order, which involves the computation of weighted partial derivatives; the method is also
276 known as minimum mean square estimator (MMSE) (Gommenginger et al., 2011; Zanife
277 et al., 2003).

278 ALES adopts an unweighted least-square estimator whose convergence is sought through
279 the Nelder-Mead (NM) algorithm. NM is a simplex optimization method that does not
280 use the derivatives of its cost function, whilst it searches for the minimum in a many-
281 dimensional space. Specifically, considering m parameters to be estimated, given that
282 a simplex of dimension m is a polytope of the same dimension and with $m+1$ vertices
283 characterised by $m+1$ cost function values, NM generates at each step a new point whose
284 cost function is compared with its value at the vertices. If it is smaller, the point be-
285 comes a vertex of the new simplex and a new iteration is generated (Nelder & Mead,
286 1965). Convergence is reached when the diameter of the simplex is smaller than a spec-
287 ified tolerance, set at $1 \times 10^{(-10)}$ in this study. For ALES, 600 is the maximum number
288 (Nmax) of iterations allowed to reach the tolerance. As already demonstrated in Halimi
289 et al. (2012), the method is also very effective in terms of speed: the average CPU time
290 needed to process each oceanic waveform with the MATLAB code generated for ALES is

291 of the order of 0.1 seconds; the drawback of avoiding a waveform classification is that it
292 can take up to few seconds for each waveform where no clear leading edge is detectable,
293 such as on land.

294 Previous studies such as Olsson & Nelson (1975) have shown the properties of NM, and
295 Halimi et al. (2012) examined the root mean square error in the parameter estimation for
296 Brown retracking and found better performances compared with the Newton-Raphson
297 strategy, which is also an iterative method based on the derivatives such as MMSE.
298 The downside is that NM does not provide the Fisher information matrix to assess the
299 confidence interval of the fitted parameters, nevertheless an evaluation can be performed
300 by comparing the reconstructed waveform with the original returned echo (Halimi et al.,
301 2012).

302 *3.3. ALES strategy*

303 Initially, each waveform is normalised by the maximum value of an 8-point average
304 computed at each gate. Then, ALES performs the fitting in two passes; first it detects the
305 leading edge of the waveform, as explained in 3.3.1 below, and computes a first estimate of
306 τ , SWH and σ^0 by fitting the model in 3.1 to the leading-edge; the SWH value is used as
307 explained in 3.3.2 to select a SWH-dependent subwaveform window on which to perform
308 a more precise estimate of the three parameters in the second pass of the algorithm. A
309 flow diagram of the main steps followed by ALES to retrack each waveform is shown in
310 figure 4. For brevity we will refer to the start gate number and end gate number of the
311 sub-waveform window as the startgate and stopgate, respectively. A subwaveform will
312 therefore be defined as the part of the waveforms whose first and last gates are identified
313 by startgate and stopgate.

314 *3.3.1. First pass: leading edge detection and fitting*

315 The first estimation is performed on a window that includes the leading edge of the
316 echo, entirely excluding the trailing edge.

317 Thermal noise is estimated from an average of the first few gates and removed from
318 the signal. For Envisat, gates 5 to 10 are chosen, since the first gates are affected by
319 aliasing due to the application of a digital filter that wraps around the high frequency
320 components of the received pulse into the low frequency waveform samples. In Jason-1
321 and Jason- 2, the first and the last gates are already excluded from the waveforms (104

322 gates are given, rather than the full 128 as in Envisat), therefore we estimate thermal
323 noise from the average of gates 1 to 5. For the same reason, ALES startgate is gate 5 for
324 Envisat and gate 1 for Jason-1 and Jason-2.

325 The main leading edge detection is based on the difference between consecutive gates.
326 The algorithm searches for the beginning of the leading edge (edge foot): this is taken
327 to be the first gate where the difference of two consecutive gates is positive and greater
328 than 1% of the normalization factor, i.e. when:

$$Dwf > 0.01 \quad (2)$$

329 where Dwf is the vector containing the differences between consecutive gates and
330 numbers are expressed in normalised power units. The 1% threshold is arbitrary and it
331 is defined to detect the reception of a return echo.

332 Then the algorithm finds the end of the main leading edge (edge top) at the first
333 following gate where the difference of consecutive waveform values becomes negative, i.e.
334 when:

$$Dwf < 0 \quad (3)$$

335 The stopgate for this first pass is taken as the edge top gate plus one. Due to noise,
336 the exact location of the end of a leading edge is not precisely defined in a waveform.
337 This can lead to a problem of accuracy in the case of a simple leading-edge retracker.
338 However, the stopgate is here only used to define the subwaveform for the first estimation
339 of Epoch and SWH, whose final values are the result of the second estimation, which is
340 independent of the stopgate.

341 Returns from discrete raised surfaces, such as the decks of ships, can sometimes be seen
342 as small power spikes in the gates preceding the leading edge. These can be erroneously
343 detected as leading edges according to criterion 2. To avoid such erroneous detections,
344 edges whose power drops below 10% of the normalisation factor within 4 gates from the
345 edge top are excluded.

346 The subwaveform is then fitted as in section 3.2. When convergence is not reached in
347 N_{max} iterations, the estimation window is widened by increasing the stopgate by 1 (i.e.
348 widening the window towards the waveform tail), and so on, until convergence is reached.

349 Epoch and SWH from the leading edge sub-waveform estimation are then used to
350 select a wider sub-waveform for the second pass.

351 *3.3.2. Second pass: selection of sub-waveform and precise final estimation*

352 For best accuracy the subwaveform width for the second pass must be optimised such
353 that it fully includes all gates comprising the leading edge, but with minimal contribu-
354 tion from the trailing edge, where artefacts such as bright target responses may prevent
355 equation 1 from accurately describing the shape. In effect the issue is one of defining
356 an appropriate stopgate for the second pass retracking based upon the SWH estimates
357 from the first pass. The relationship between SWH and stopgate was derived from Mon-
358 tecarlo simulations. For each value of SWH ranging from 0.5 to 10 m in steps of 0.5 m,
359 500 high-rate waveforms were simulated with the model in 3.1 adding realistic Rayleigh
360 noise. The resulting waveforms were retracked using the classic Brown-Hayne model in
361 3.1 over the entire waveform, and then over sub-waveform windows with startgate=1 and
362 variable stopgate, and the RMS errors (RMSE) computed.

363 The difference of the RMSEs between the "full waveform" estimate and the sub-
364 waveform estimates is displayed in figure 5 as a function of the stopgate position. Upper
365 left, upper right and lower left panels show the results for Epoch, SWH and amplitude
366 estimation. The x axis is, in practice, the width of the sub-waveform, expressed as number
367 of gates from the tracking point to the stopgate. The results for each SWH level are coded
368 in different colours. For all three parameters, the curves converge asymptotically to the
369 full waveform estimates, as expected for this idealised case of "pure-Brown" response of
370 the ocean surface. The amplitude is the parameter that needs the smallest amount of
371 gates to be properly estimated - and indeed in some cases its estimate can be marginally
372 more accurate by discarding part of the tails, as indicated by the positive difference of
373 RMSEs. Epoch and SWH estimations show similar patterns, although the curves are less
374 smooth for the SWH. This is also expected, since SWH retrieval is normally noisier in
375 the retracking of real waveforms. In the lower right panel, a linear relationship is derived
376 between SWH and the number of gates needed using a 1 cm RMSE tolerance compared
377 to the theoretical precision of a "full waveform" estimation. The choice of the 1 cm
378 tolerance is a trade off between retaining an "open-ocean" level of precision and avoiding
379 perturbations in the trailing edge. We consider 1 cm a good compromise since it is much
380 less than the estimated noise on high rate range measurements found in previous studies

381 on Jason-1, Jason-2 and Envisat (Faugere et al., 2006; Thibaut et al., 2010).

382 The parameters h , θ_0 and σ_p (defined in section 3.1) change depending on the mission.
383 Therefore the same Montecarlo simulation was run for both Envisat and Jason, resulting
384 in slightly different coefficients of the linear relationship derived (figure 4 refers to Envisat)
385 . From these results, the stopgate of the ALES estimation window is calculated using the
386 following equations:

$$\text{Maximum gate} = \text{Ceiling}(\text{Tracking point} + 2.4263 + 4.1759 \times \text{SWH}) \quad (4)$$

387 for Envisat and

$$\text{Maximum gate} = \text{Ceiling}(\text{Tracking point} + 1.3737 + 4.5098 \times \text{SWH}) \quad (5)$$

388 for Jason-1 and Jason-2.

389 where tracking point and SWH are from the first pass. The final estimation of the
390 three parameters τ , SWH and σ^0 is made from this window width at the second pass.

391 Examples of three typical fittings of real waveforms (blue line) by ALES (dashed red
392 line) are provided in figure 6 for open ocean with low SWH, coastal ocean with corrupted
393 trailing edge and open ocean with high SWH.

394 3.3.3. *Mispointing angle*

395 Every radar altimeter has a degree of inaccuracy in pointing perpendicular to the
396 ocean surface. The slope of the trailing edge in the theoretical Brown functional form
397 depends on the mispointing angle, which measures how much the antenna pointing devi-
398 ates from nadir. The most significant effect is in the estimation of the signal amplitude,
399 reducing the apparent backscatter coefficient (Wingham, 1988; Quartly, 2009).

400 In its current version, ALES does not estimate mispointing. Values are taken from the
401 SGDR products. In standard three-parameter retracking, such as for Envisat, the angle
402 is computed from the slope of the logarithm of the trailing edge (Amarouche et al., 2004).
403 In the current version of Jason-1 and Jason-2 SGDR, the mispointing is estimated in the
404 retracking process (from the MLE4 retracker) together with Epoch, SWH and amplitude.
405 We use this output as input for our three-parameter model, and this should not influence
406 the correct range retrieval for angles smaller than 0.3° (Dorandeu et al., 2004). Where no

407 estimate from the SGDR is available, for example where SGDR retracking failed, we take
 408 the last valid measurement. The mispointing values are then smoothed over 3 seconds.
 409 These are reasonable approximations considering that Amarouche et al. (2004) suggested
 410 that a smoothing over 30 seconds should be applied when mispointing is calculated from
 411 the waveform. It is therefore appropriate to always smooth the value for the mispointing
 412 to avoid features in the trailing edge affecting ALES performance through the mispointing
 413 values used.

414 4. Validation and discussion

415 This section presents the validation of ALES range retrieval. To check the data
 416 quality, time series of sea level variability measured from altimetry and tide gauges can
 417 be compared by analysing correlation and root mean square (RMS) (Fenoglio-Marc et al.,
 418 2010). The variable that we extracted for the comparison is the Total Water Level
 419 Envelope (TWLE), defined as:

$$\text{TWLE} = \text{Orbit altitude} - \text{Corrected Range} - \text{Mean Sea Surface} - (\text{Solid Earth Tide} + \text{Load Tide}) \quad (6)$$

420 where

$$\begin{aligned} \text{Corrected Range} = & \text{Range} + \text{Instrumental corrections} + \text{Dry tropospheric correction} + \\ & \text{Wet Tropospheric Correction} + \text{Sea State Bias} + \text{Ionospheric correction} \end{aligned} \quad (7)$$

421 TWLE represents the combined effect of ocean tides and atmospheric forcing in ad-
 422 dition to the sea level anomaly with respect to the mean sea surface. It is therefore
 423 particularly useful for applications that need an estimate of the total sea level above the
 424 mean, such as the analysis of storm surges. The DTU10 mean sea surface (Andersen,
 425 2010) was subtracted from the retrieved sea surface height for all the tracks. In order
 426 to compare the altimeter data with the TGs, the effect of atmospheric pressure on the
 427 sea level was not applied to either dataset (Fenoglio-Marc et al., 2004). While Envisat
 428 and Jason-1 SGDR provide estimations of the range from a single oceanic retracker, the
 429 latest version of Jason-2 gives two estimations for each waveform, coming from MLE3
 430 and MLE4 retrackers (Thibaut et al., 2010). To be consistent with the comparison with
 431 Jason-1, only the MLE4 estimates for Jason-2 are used in this study.

432 A numerical summary of the comparative analysis with the tide gauges for each track
433 is presented in table 2. The outliers are defined according to section 4.2. For each track,
434 the median value of the along-track correlation is shown. For J-2 198 and Env 687 in
435 Mossel Bay (figure 3), since there was no independent estimate of TG height relative
436 to the ellipsoid, RMS values correspond to the median value of the along-track RMS of
437 the difference between TWLE and TG sea level height anomaly (with the mean of the
438 difference removed), while for J-2 196, J-1 161 and Env 416 in the Adriatic Sea we report
439 the RMS of the difference of the absolute sea level heights above the ellipsoid at the
440 closest point between TG and satellite tracks. The altimetric absolute sea level heights
441 are obtained by adding the mean sea surface to the TWLE defined in equation 6.

442 *4.1. Validation of raw data*

443 The first validation test was performed on all the available along-track range estima-
444 tions from both SGDR and ALES. The aim was to determine for each latitude longitude
445 location the maximum number of cycles of data that could be retained whilst guaran-
446 teeing a correlation with the TG time series of at least 0.9. The test was performed in
447 an iterative way: for each location, the correlation of the TG time series with the entire
448 set of altimetry retrievals was checked; if the correlation coefficient was lower than 0.9,
449 then the cycle with the maximum discrepancy between TG value and altimeter retrieval
450 was excluded. The output assesses the general quality of the retracked altimetry values
451 against the available SGDR product. It is important to perform the analysis before any
452 outliers exclusion, in order to quantitatively evaluate whether ALES, compared to stan-
453 dard products, can provide a higher number of accurate estimations at each location.
454 The same analysis was performed for CTOH 1-Hz locations.

455 Figure 7 and 8 show the results for the tracks in the Adriatic and the tracks near South
456 Africa. Land areas are shaded in grey. The x-axis represents the along-track progression
457 of each track in latitude. The latitude of the tide gauge is specified by a black dot. Red
458 squares characterise the ALES dataset, while SGDR products are in blue squares and
459 CTOH points are seen as cyan dots. The distance from the closest coastline is specified
460 by a green line which refers to the y-axis on the right.

461 Env 416 height retrieval is particularly problematic in the gulf area, between 45.5
462 and 45.8° N. Here ALES shows improvements particularly in the sea-to-land transition,
463 with over 60% of cycles highly correlated in locations closer than 2.5 km to the coast,

464 where the amount of highly correlated cycles in the SGDR product decrease significantly.
465 After roughly 3.7 km from the stretch of land in Istria, both ALES and SGDR have more
466 than 80% of cycles highly correlated, but along the rest of the track ALES constantly
467 maintains a higher percentage.

468 The improvement of data quality in the gulf area is even more evident considering
469 J-1 161. The percentage of ALES highly correlated cycles is constantly well above 60%,
470 a threshold that is hardly overtaken by SGDR in the same locations. Before the Istrian
471 stretch, availability of good ALES data is constantly over 80% of the cycles until 2.5 km
472 from the coast, while the percentage for the SGDR drops below 80% by 7 km from the
473 Istrian peninsula. For both J-1 161 and Env 416 in the Gulf of Trieste, CTOH had no
474 data for any cycle. The first available measurements are situated more than 10 km along-
475 track from the Istrian peninsula and several cycles contained empty data, as evident by
476 the low percentage in the figure.

477 Along the descending J-2 196 track, ALES retrieves more than 80% of highly corre-
478 lated cycles within 7 km along-track from the islet that marks the beginning of the lagoon
479 (visible on the plot as a dashed black vertical line), while the SGDR data take 13 km
480 (along-track distance) to get to a comparable level. It is particularly striking how ALES
481 is also able to capture more valid data also inside the lagoon, showing that ALES could
482 potentially be used for inland water sea level measurements.

483 In the tracks that pass over South Africa, which fly over a wide open ocean area,
484 the results for SGDR and ALES are extremely similar. Nevertheless the performances
485 of SGDR slightly decrease at 11 km from the coast, while ALES points are highly cor-
486 related to within 1.5 km. Along J-2 198, the parallel degradation of the two datasets
487 in proximity to the coast is explained by failure of the Jason on-board tracker, an event
488 that particularly occurs in the transition from land to sea (Brooks et al., 1998).

489 *4.2. Outlier detection*

490 In order to further analyse the correlation and the RMS between in-situ sea level
491 observations and ALES estimations, outliers have been detected and excluded. Validity
492 does not imply accuracy and therefore the number of valid points does not correspond
493 to the total number of "correct" estimates; nevertheless the outlier detection is applied
494 to exclude extreme values of ALES output which would alter the correlation and RMS
495 analysis performed on the full time series.

496 For the sake of comparison, the same flagging criteria have been used for both SGDR
497 and ALES data. It is preferable to use separate quality control for each of the three
498 retracked parameters (TWLE, SWH and σ^0) in order to exclude as many poor estimations
499 as possible. Although a flag on TWLE is not suggested in the SGDR and ocean tides are
500 not removed from this quantity, tidal signal is available from the tide gauges. Therefore
501 a specific flag has been derived for this research taking into account the suggested flag for
502 sea level anomaly in the Envisat product. SWH and σ^0 suggested flagging criteria are the
503 same as the ones used for both Envisat and Jason products (Picot et al., 2003; Soussi &
504 Femenias, 2006). Table 4 lists and describes the adopted flagging criteria used for outlier
505 detection. For Envisat, since the SGDR product does not provide the high-rate values of
506 SWH and σ^0 , only the flag on TWLE could be applied.

507 Figures 9 and 10 show the along-track distribution of outliers in the two considered
508 regions. The most problematic area is the Gulf of Trieste and the reason lies in the
509 fact that a large part of these tracks is closer than 10 km from the coastline (with
510 multiple transitions from land to sea and sea to land), where the majority of Jason
511 SGDR estimations are outliers. Envisat has the smallest number of outliers among the
512 different missions. It must also be noticed that SGDR in the Adriatic has more valid
513 points than ALES. Considering the low correlation of SGDR (see section 4.3) along this
514 track in the locations where the outliers are less than for ALES, we conclude that some
515 of the SGDR poor estimations are not extreme enough to be eliminated by the outliers
516 detection.

517 Since in Jason missions the outlier detection can be extended to SWH and σ^0 , we
518 assume this comparison to be more meaningful. In J-1 161 ALES succeeds in keeping the
519 outliers below 25% even very close to the coastline, where SGDR exceeds 60%. In J-2 196
520 the number of ALES outliers is almost always less than the number of SGDR outliers,
521 and between 45.6 and 45.7 °N there are less than 20% outliers, whereas SGDR reaches
522 over 60%. In J-2 198 the percentage of outliers rises in the last 6 km from the coastline,
523 at the same pace both in SGDR and in ALES. Here waveforms are highly corrupted and a
524 leading edge is difficult to recognise, as a result of the problematic land-to-sea transition
525 of the Jason altimeter.

526 It has already been said that erroneous estimations are due to waveforms that do
527 not conform to the Brown model, among which those with a moving bright target in the

528 trailing edge are common in coastal areas, as showed in previous studies such as Halimi
529 et al. (2012), where waveforms are classified according to their shape. We argue that the
530 higher percentage of outliers in the Gulf of Trieste compared to Mossel Bay is connected
531 with the shape of the coastline and its influence on the sea state. Depending on wind
532 intensity and direction in the Gulf of Trieste the rugged coastline can create patches of
533 sheltered calm water visible as bright targets in the radargrams, such as the ones of figure
534 2. Further explanation must be found in the analysis of the wind direction, frequency and
535 intensity, but also of the wave height and in the interaction between wind and currents,
536 since all these factors affect the sea surface roughness (Lange et al., 2004). Moreover,
537 film slicks on the sea surface are common in the coastal ocean and are mainly related to
538 surfactant accumulation and upwelling fronts (Ermakov et al., 1992; Ryan et al., 2010).
539 They can extend for many kilometres in calm conditions and create patches of very low
540 surface roughness that can be seen as bright targets in the radar signal. Oil slicks from
541 ships are also to be investigated as a source of highly reflective water: both North Adriatic
542 and South African coasts have high shipping activity, but the slow surface currents of
543 the Adriatic and in particular of the Gulf of Trieste might enhance the permanence of
544 the slicks in that area. Phytoplankton blooms can also have a strong effect, but their
545 signal would be highly seasonal and more sporadic than the observed recurrence of bright
546 targets.

547 *4.3. Correlation coefficient*

548 Once the outliers were removed, the correlation between ALES TWLE and TG was
549 computed. For comparison, the correlation coefficient (r) was also computed for SGDR
550 output from the same waveforms. As table 1 shows, SGDR data display missing values
551 in locations where waveforms are present. For each location, in order to produce an
552 unbiased comparison, we only consider correlation when both SGDR and ALES estimates
553 are available.

554 Along-track spatial variation of r for the different tracks is displayed in figures 11 and
555 12. ALES improvement in correlation compared to SGDR is widespread. In the open
556 seas, r for ALES is constantly over 0.8, with a few drops that may be due to undetected
557 erroneous TWLE estimations, but may also be due to imprecise corrections when the
558 drops are seen also in r for SGDR. In the Gulf of Trieste, r for ALES is always higher
559 than for SGDR for distances greater r than 2.5 km from the coastline, and it is always

560 above 0.6 for J-1 161 and J-2 196. The low values of r for Env 416 suggest that a more
561 careful quality control of the estimations will be necessary in a post-processing phase; for
562 example, separate quality control of the SWH and σ^0 estimations, which has not been
563 done in this study for Envisat due to the lack of 20Hz estimations in the SGDR product,
564 as explained in the previous section.

565 Env 687 in South Africa presents a steady high correlation of over 0.9 until within 2.5
566 km of coastline, but the SGDR data have a significant drop between 10 km and 5 km
567 from the coastline, a degradation that is not seen in ALES data. Along J-2 198 SGDR
568 data also have a drop at 10 km from the coastline, while ALES maintains r above 0.8.
569 ALES presents a single low r value in the open ocean, a closer investigation of this case
570 revealed the presence of a false leading edge, indicating a future area for improvement in
571 the routine described in section 3.3.1.

572 The comparison with CTOH data is extremely promising: ALES data have the same
573 level of correlation with the tide gauges despite being a high-rate non-filtered product.
574 A higher correlation of the tide gauges with CTOH 1-Hz data was expected as these
575 data have already been post-processed and therefore outliers have been excluded in the
576 calculation of 1-Hz mean from the 20 Hz measurements. Reaching the same correlation
577 as CTOH values without any filtering or selection means that high rate values with
578 appropriate flagging can be effectively used to produce altimetric data at finer resolutions
579 and in addition areas where no CTOH output is available, such as the innermost part of
580 the Gulf of Trieste, can still be described by ALES with unprecedented accuracy.

581 *4.4. Root Mean Square Difference*

582 The absolute validation against coastal tide gauges in terms of sea level can help to
583 assess whether the comparability between in-situ data and altimetry is increased by the
584 use of improved retracking strategies. Figure 12 shows the RMS of the difference (RMSD)
585 between the time series of the absolute sea level height above the ellipsoid WGS84 (major
586 radius $a=6378137$ m, flattening $f=298.257223563$) for the tracks in the North Adriatic
587 and the equivalent time series at Trieste TG. Since the reference ellipsoid of the satel-
588 lite altitude in Jason and DTU10 mean sea surface is TOPEX ellipsoid (major radius
589 $a=6378136.3$ m, flattening $f=298.257$), values are corrected for the difference between
590 the two ellipsoid models in order to refer each parameter to WGS84. The heights from
591 satellite altimetry are also corrected for the absolute biases found in Bonnefond et al.

592 (2013).

593 Minimum RMSD values are expected to be found using the along-track point near-
594 est to the TG, although this depends on the slope of the local geoid and local currents.
595 Heights measured by the tide gauges and by the altimeters are always different since the
596 altimeters do not fly exactly over the tide gauge and the tide gauge is a point measure-
597 ment, while a radar altimeter considers the entire footprint. For a more precise estimation,
598 altimetry calibration processes take into account the difference in geoid height between the
599 track and the TG, but this is done only at dedicated sites where regional high-resolution
600 geoid models are available (Bonnetfond et al., 2011). Moreover even presently available
601 high-resolution global geoid models (such as EGM08) are not suitable for this purpose
602 in proximity of the coast (within 20 km) (Bonnetfond et al., 2012). In our comparative
603 analysis we do not aim to calibrate a sensor and we therefore do not apply a correction
604 for geoid gradient. However, to help the evaluation, figure 13 also includes the difference
605 between the DTU10 mean sea surface at the TG and the along-track.

606 In the open Adriatic, ALES RMSD values decrease steadily towards the tide gauge for
607 Env 416 and for J-1 161, with worsening performances for Env 416 in the last 2.5 km. In
608 the gulf, RMSD values are more variable, in particular for Env 416, but the comparison
609 with the SGDR output for the same waveforms highlights the improvements of our new
610 retracking system. For J-2 196, the absolute RMSD is more difficult to evaluate, because
611 of the greater distance (over 30 km at the closest point) from the tide gauge. ALES
612 RMSD accurately follows this shape from 4 km of distance from the Istrian coast until
613 the proximity of the lagoon, in locations where SGDR values are extremely different from
614 the tide gauge measurements.

615 Since the ellipsoidal height of Mossel Bay TG was not available, a relative analysis
616 was performed by computing the RMS of the difference between TWLE and tide gauge
617 values. The results are shown in figure 14 and are very comparable to the correlation
618 analysis.

619 *4.5. Distribution and bias analysis*

620 One of the main aims of this study was to assess the validity of the same retracker for
621 both open ocean and coastal data. It is important therefore that the high rate estimations
622 of the new retracker are not noisier than the standard SGDR product. We consider the
623 differences between consecutive high-rate TWLE values as a good estimation of noise,

624 since TWLE is not supposed to change significantly in 300 to 350 metres, which is the
625 distance between one measurement and the next.

626 TWLE consecutive differences were computed for ALES, once the outliers had been
627 removed. For comparison, the same calculation was performed for SGDR for the same
628 waveforms. The histograms of consecutive absolute differences of TWLE are shown for
629 each track in figure 15. Table 4 describes the characteristics of the distributions in terms
630 of mean, standard deviation and percentiles (1st and 99th of the whole probability density
631 function).

632 The majority of consecutive differences for both SGDR and ALES are below 10 cm,
633 which is in agreement with the high rate noise figures found in previous studies, such as
634 Zanife et al. (2003). In the Adriatic Sea, ALES is less noisy than the SGDR, an improve-
635 ment that becomes significant in J-2 196, due to the fact that most of the considered
636 short track passes over coastal waters, where SGDR performances are degraded, as seen
637 previously. Considering the tracks near South Africa, the situation changes because this
638 is an area where high significant wave height are often observed: the consequence is a
639 lower percentage of consecutive differences below 10 cm for both SGDR and ALES com-
640 pared to the tracks in the Adriatic Sea. ALES is slightly more affected by high SWH
641 conditions compared to the SGDR product in terms of noise, particularly for J-2 198.
642 This is also observable in the percentile interval, which is 3 cm wider for ALES in the
643 same track.

644 The percentile interval is significantly wider for SGDR in the Adriatic sea, which
645 confirms that the outliers detection performed on ALES successfully eliminates most of
646 the incorrect estimations. ALES mean and standard deviation of the distributions also
647 show values similar to SGDR, with an improvement for J-1 161 and J-2 196, which are
648 the two tracks where SGDR output showed the most significant degradation.

649 Biases between SGDR and ALES were also estimated for each track. Values were
650 averaged only at those along-track points where raw data showed a correlation with the
651 TGs higher than 0.9 for both SGDR and ALES TWLE and at least 50% of valid points
652 were available for both the datasets, therefore no bias was computed for J-2 196, where
653 no SGDR along-track points were so well correlated. Results are presented in table 5.
654 Biases are of the order of 1 cm, with standard deviations of the order of 2 to 5 cm. These
655 low values show how ALES constitutes a coastal-dedicated improvement of the standard

656 oceanic product without a significant loss of comparability with the SGDR estimation.

657 **5. Conclusion**

658 The present study aimed at the development and validation of ALES, the Adaptive
659 Leading Edge Subwaveform retracker, which is capable of retrieving useful sea level infor-
660 mation both in the open ocean and in the coastal zone. ALES estimates the parameters
661 of interest while disregarding most of the trailing edge of a waveform, which is where
662 deviations from the open ocean Brown model affect the quality of the standard altimetry
663 product. The algorithm is based on a two-pass retracking which at first is only focused
664 on the leading edge and then extends the estimation window including a variable number
665 of gates depending on the SWH, in order try to ensure the same level of precision.

666 The retracker has been validated for Jason-1, Jason-2 and Envisat in two very dif-
667 ferent oceanographic areas. The results show on one hand that there is no significant
668 degradation between standard open ocean high-rate TWLE estimation and ALES values
669 in terms of noise and accuracy and on the other hand that ALES significantly increases
670 the amount of altimetric information retrievable in the coastal zone, in areas that were
671 disregarded even by dedicated coastal post-processed datasets, such as in the Gulf of
672 Trieste.

673 It is very important to stress that the benefits are not limited to a 10 km wide strip
674 along the coast, where the satellite footprint assimilates land return together with ocean
675 signal, but extend to tens of kilometres from the coast. Deviations from the standard
676 open ocean model are seen much further in the open sea, because land interference is not
677 the main source of perturbation in the trailing edge. Bright targets are mainly connected
678 to sea state and areas of low sea roughness that can be caused by land sheltering from
679 winds or coastal upwelling fronts that produce film slicks on the surface.

680 ALES improves the quantity and the quality of coastal altimetry data without adding
681 significant further noise to the estimation. Biases of the order of 1 cm with SGDR
682 values demonstrate the comparability between the two datasets. Further analysis on bias
683 and noise is needed and will be performed once an extensive global retracked dataset is
684 available.

685 A dedicated quality control, independent from the comparison with SGDR, is needed
686 in order to generate a consistent final product. Correlation and RMS analysis show that,

687 with proper removal of outliers, high-rate data are as accurate as 1-Hz post-processed sea
688 level heights. A quality criterion based also on the differences of consecutive estimates
689 can help the selection of data with low noise in order to avoid the need to average to
690 1-Hz, which limits the availability of measurements to one point roughly every 7 km.
691 Applications such as data assimilation into models and coastal circulation studies would
692 highly benefit from fine resolution coastal altimetry measurements.

693 The possibility to have a multi-mission retracker opens a wide range of further studies
694 in terms of applications and extensions. Validation with TG data also demonstrates that
695 ALES can be used for coastal sea level and surge monitoring studies, due to its increased
696 comparability with the coastal in-situ sensors. Recent studies such as Masina & Lamberti
697 (2013) demonstrate that there is interest in extreme sea level monitoring in the Northern
698 Adriatic, where ALES has been validated and could be used to improve the available
699 observations. ALES also retrieves SWH and σ^0 and further research is needed to validate
700 these parameters against in-situ data.

701 The effort of the research on retracking should of course be assisted by new coastal-
702 dedicated corrections, in particular wet troposphere correction and sea state bias, and,
703 where possible, regional high resolution tidal models, in order to isolate the sea level
704 anomaly from the TWLE. Once SWH and σ^0 are validated, sea state bias correction can
705 be improved using ALES estimates.

706 ALES should also be applied to previous (TOPEX,ERS) and present pulse-limited
707 altimetry missions (Alti-Ka, HY-2) to extend the time-series and realise the improvement
708 brought by the new altimeters and their smaller footprint.

709 **Acknowledgements**

710 We want to thank ISPRA (Istituto Superiore per la Protezione e la Ricerca Ambien-
711 tale) for providing sea level measurements from the tide gauge in Trieste. Special thanks
712 go to: Francesco De Biasio (CNR-ISMAR) for his help and assistance; Yang Le and Bao Li
713 Feng for sharing their algorithms; Luciana Fenoglio, Abderrahim Halimi, Walter Smith,
714 Luke West and Phil Woodworth for their suggestions. This work has been partially sup-
715 ported by the ESA/DUE eSurge (ESA/ESRIN Contract Number 4000103880/11/I-LG)
716 and eSurge-Venice (ESA/ESRIN Contract No. 4000104485/11/I-LG) projects.

717 **References**

- 718 Amarouche, L., Thibaut, P., Zanife, O., Dumont, J.-P., Vincent, P., & Steunou, N.
719 (2004). Improving the Jason-1 ground retracking to better account for attitude effects.
720 *Marine Geodesy*, *27*, 171–197.
- 721 Andersen, O. (2010). The DTU10 gravity field and mean sea surface. In *Second interna-*
722 *tional symposium of the gravity field of the Earth (IGFS2)*. Univ. of Alaska Fairbanks,
723 Fairbanks.
- 724 Andersen, O., Knudsen, P., & Berry, P. (2010). The DNSC08GRA global marine gravity
725 field from double retracked satellite altimetry. *Journal of Geodesy*, *84*, 191–199.
- 726 Bao, L., Lu, Y., & Wang, Y. (2009). Improved retracking algorithm for oceanic altimeter
727 waveforms. *Progress in Natural Science*, *19*, 195–203.
- 728 Becker, M., Zerbini, S., Baker, T., Bürki, B., Galanis, J., Garate, J., Georgiev, I., Kahle,
729 H.-G., Kotzev, V., & Lobazov, V. (2002). Assessment of height variations by GPS at
730 Mediterranean and Black Sea coast tide gauges from the SELF projects. *Global and*
731 *Planetary Change*, *34*, 5–35.
- 732 Berry, P., Bracke, H., & Jasper, A. (1997). Retracking ERS-1 altimeter waveforms over
733 land for topographic height determination: an expert systems approach. *ESA-SP 414*,
734 *3rd ERS Symposium, Florence, Italy, (17-20 March 1997)*, *414*, 403–408.
- 735 Berry, P., Freeman, J., & Smith, R. (2010). An enhanced ocean and coastal zone retrack-
736 ing technique for gravity field computation. In S. Mertikas (Ed.), *Gravity, Geoid and*
737 *Earth Observation* (pp. 213–220). Berlin Heidelberg: Springer-Verlag.
- 738 Birol, F., Cancet, M., & Estournel, C. (2010). Aspects of the seasonal variability of the
739 northern current (NW Mediterranean Sea) observed by altimetry. *Journal of Marine*
740 *Systems*, *81*, 297–311.
- 741 Bonnefond, P., Exertier, P., Laurain, O., T., G., & Femenias, P. (2013). Corsica: a
742 multi-mission absolute calibration site. In *Proceeding of '20 Years of Progress in Radar*
743 *Altimetry* ESA-SP-710.

- 744 Bonnefond, P., Exertier, P., Laurain, O., Thibaut, P., & Mercier, F. (2012). GPS-based
745 sea level measurements to help the characterization of land contamination in coastal
746 areas. *Advances in Space Research*, *51*, 1383–1399.
- 747 Bonnefond, P., Haines, B., & Watson, C. (2011). In situ absolute calibration and vali-
748 dation: a link from coastal to open-ocean altimetry. In S. Vignudelli, A. Kostianoy,
749 P. Cipollini, & J. Benveniste (Eds.), *Coastal Altimetry* (pp. 259–96). Berlin Heidelberg:
750 Springer-Verlag.
- 751 Bouffard, J., Roblou, L., Birol, F., Pascual, A., Fenoglio-Marc, L., Cancet, M., Morrow,
752 R., & Menard, Y. (2011). Introduction and assessment of improved coastal altimetry
753 strategies: case study over the Northwestern Mediterranean Sea. In S. Vignudelli,
754 A. Kostianoy, P. Cipollini, & J. Benveniste (Eds.), *Coastal Altimetry* (pp. 297–330).
755 Berlin Heidelberg: Springer-Verlag.
- 756 Boyd, A., & Shillington, F. (1994). Physical forcing and circulation patterns on the
757 Agulhas Bank. *South African Journal of Science*, *90*, 114–114.
- 758 Brooks, R. L., Lockwood, D. W., Lee, J. E., Handcock, D., & Hayne, G. S. (1998). Land
759 effects on TOPEX radar altimeter measurements in Pacific Rim coastal zones. *Remote*
760 *Sensing of the Pacific by Satellites*, edited by RA Brown, (pp. 175–198).
- 761 Brown, G. (1977). The average impulse response of a rough surface and its applications.
762 *IEEE Transactions on Antennas and Propagation*, *25*, 67–74.
- 763 Chelton, D. B., Ries, J. C., Haines, B. J., Fu, L.-L., & Callahan, P. S. (2001). Satellite
764 altimetry. *International Geophysics*, *69*, 1–131.
- 765 Deng, X., & Featherstone, W. (2006). A coastal retracking system for satellite radar
766 altimeter waveforms: application to ERS-2 around Australia. *Journal of Geophysical*
767 *Research*, *111*, C06012.
- 768 Deng, X., Featherstone, W., Hwang, C., & Berry, P. (2002). Estimation of contamination
769 of ERS-2 and Poseidon satellite radar altimetry close to the coasts of Australia. *Marine*
770 *Geodesy*, *25*, 249–271.

- 771 Dorandeu, J., Ablain, M., Faugere, Y., Mertz, F., Soussi, B., & Vincent, P. (2004). Jason-
772 1 global statistical evaluation and performance assessment: Calibration and cross-
773 calibration results. *Marine Geodesy*, *27*, 345–372.
- 774 Dussurget, R., Birol, F., Morrow, R., & De Mey, P. (2011). Fine resolution altimetry
775 data for a regional application in the Bay of Biscay. *Marine Geodesy*, *34*, 447–476.
- 776 Ermakov, S., Salashin, S., & Panchenko, A. (1992). Film slicks on the sea surface and
777 some mechanisms of their formation. *Dynamics of Atmospheres and Oceans*, *16*, 279–
778 304.
- 779 Faugere, Y., Dorandeu, J., Lefevre, F., Picot, N., & Femenias, P. (2006). Envisat ocean
780 altimetry performance assessment and cross-calibration. *Sensors*, *6*, 100–130.
- 781 Fenoglio-Marc, L., Dietz, C., & Groten, E. (2004). Vertical land motion in the Mediter-
782 ranean Sea from altimetry and tide gauge stations. *Marine Geodesy*, *27*, 683–701.
- 783 Fenoglio-Marc, L., Fehla, M., Ferri, L., Becker, M., Gao, Y., & Vignudelli, S. (2010).
784 Coastal sea surface heights from improved altimeter data in the Mediterranean Sea. In
785 *Gravity, Geoid and Earth Observation* (pp. 253–261). Springer.
- 786 Ferrari, R., Provost, C., Sennéchaël, N., & Lee, J.-H. (2013). Circulation in Drake
787 Passage revisited using new current time series and satellite altimetry: 2. The Ona
788 basin. *Journal of Geophysical Research: Oceans*, *117*.
- 789 Ferrarin, C., Umgiesser, G., Scroccaro, I., & Matassi, G. (2009). Hydrodynamic modeling
790 of the lagoons of Marano and Grado, Italy. *ISMAR, ARPA*, .
- 791 Gamboni, E. (1965). Sul caposaldo fondamentale di riferimento della nuova rete altimet-
792 rica di alta precisione. *Bollettino di Geodesia e Scienze Affini*, *1*, 155–165.
- 793 García, F., Vigo, M., García-García, D., & Sánchez-Reales, J. (2012). Combination of
794 multisatellite altimetry and tide gauge data for determining vertical crustal movements
795 along Northern Mediterranean Coast. *Pure and Applied Geophysics*, *169*, 1411–1423.
- 796 Gomez-Enri, J., Vignudelli, S., Quartly, G. D., Gommenginger, C. P., Cipollini, P., Chal-
797 lenor, P. G., & Benveniste, J. (2010). Modeling ENVISAT RA-2 waveforms in the

798 coastal zone: case study of calm water contamination. *IEEE Geoscience and Remote*
799 *Sensing Letters*, 7, 474–478.

800 Gommenginger, C., Thibaut, L., P. abd Fenoglio-Marc, Quartly, G. D., Deng, X., Gomez-
801 Enri, J., Challenor, P. G., & Gao, Y. (2011). Retracking altimeter waveforms near the
802 coasts. In S. Vignudelli, A. Kostianoy, P. Cipollini, & J. Benveniste (Eds.), *Coastal*
803 *Altimetry* (pp. 61–102). Berlin Heidelberg: Springer-Verlag.

804 Guo, J., Gao, Y., Hwang, C., & Sun, J. (2010). A multi-subwaveform parametric retracker
805 of the radar satellite altimetric waveform and recovery of gravity anomalies over coastal
806 oceans. *Science China Earth Sciences*, 53, 610–616.

807 Halimi, A., Mailhes, C., Tourneret, J.-Y., Thibaut, P., & Boy, F. (2012). Parameter
808 estimation for peaky altimetric waveforms. *IEEE Transactions on Geoscience and*
809 *Remote Sensing*, (pp. 1568–1577).

810 Hayne, G. S. (1980). Radar altimeter mean return waveforms from near-normal-incidence
811 ocean surface scattering. *IEEE Transactions on Antennas and Propagation*, 28, 687–
812 692.

813 Herbert, G., Ayoub, N., Marsaleix, P., & Lyard, F. (2011). Signature of the coastal
814 circulation variability in altimetric data in the southern Bay of Biscay during winter
815 and fall 2004. *Journal of Marine Systems*, 88, 139–158.

816 Hwang, C., Guo, J., Deng, X., Hsu, H.-Y., & Liu, Y. (2006). Coastal gravity anomalies
817 from retracked Geosat/GM altimetry: improvement, limitation and the role of airborne
818 gravity data. *Journal of Geodesy*, 80, 204–216.

819 Idris, N., & Deng, X. (2012). The retracking technique on multi-peak and quasi-specular
820 waveforms for Jason-1 and Jason-2 missions near the coast. *Marine Geodesy*, 35,
821 217–237.

822 Lange, B., Johnson, H., Larsen, S., Højstrup, J., Kofoed-Hansen, H., & Yelland, M.
823 (2004). On detection of a wave age dependency for the sea surface roughness. *Journal*
824 *of Physical Oceanography*, 34, 1441–1458.

825 Le Hénaff, M., Roblou, L., & Bouffard, J. (2011). Characterizing the navidad current
826 interannual variability using coastal altimetry. *Ocean Dynamics*, 61, 425–437.

- 827 Lee, H., Shum, C., Emery, W., Calmant, S., Deng, X., Kuo, C.-Y., Roesler, C., & Yi, Y.
828 (2010). Validation of Jason-2 altimeter data by waveform retracking over California
829 coastal ocean. *Marine Geodesy*, *33*, 304–316.
- 830 Liu, Y., Weisberg, R. H., Vignudelli, S., Roblou, L., & Merz, C. R. (2012). Comparison
831 of the X-TRACK altimetry estimated currents with moored ADCP and HF radar
832 observations on the West Florida Shelf. *Advances in Space Research*, *50*, 1085–1098.
- 833 Marth, P. C., Jensen, J. R., Kilgus, C. C., Perschy, J. A., MacArthur, J. L., Hancock,
834 D. W., Hayne, G. S., Purdy, C. L., Rossi, L. C., & Koblinsky, C. J. (1993). Prelaunch
835 performance of the NASA altimeter for the TOPEX/Poseidon project. *IEEE Trans-*
836 *actions on Geoscience and Remote Sensing*, *31*, 315–332.
- 837 Masina, M., & Lamberti, A. (2013). A nonstationary analysis for the Northern Adriatic
838 extreme sea levels. *Journal of Geophysical Research: Oceans*, *118*, 3999–4016.
- 839 Melet, A., Gourdeau, L., & Verron, J. (2010). Variability in Solomon Sea circulation
840 derived from altimeter sea level data. *Ocean Dynamics*, *60*, 883–900.
- 841 Mercier, F., Picot, N., Thibaut, P., Cazenave, A., Seyler, F., Kosuth, P., & Bronner,
842 E. (2009). CNES/PISTACH project: an innovative approach to get better measure-
843 ments over inland water bodies from satellite altimetry. Early results. In *EGU General*
844 *Assembly Conference Abstracts* (p. 11674). volume 11.
- 845 Nelder, J. A., & Mead, R. (1965). A simplex method for function minimization. *The*
846 *Computer Journal*, *7*, 308–313.
- 847 Olsson, D. M., & Nelson, L. S. (1975). The Nelder-Mead simplex procedure for function
848 minimization. *Technometrics*, *17*, 45–51.
- 849 Picot, N., Case, K., Desai, S., & Vincent, P. (2003). AVISO and PODAAC user handbook.
850 IGDR and GDR Jason products. *SMM_MU_M5_OP_13184_CN (AVISO) JPL D_21352*
851 *(PODAAC)*, .
- 852 Poulain, P.-M. (2001). Adriatic Sea surface circulation as derived from drifter data
853 between 1990 and 1999. *Journal of Marine Systems*, *29*, 3–32.

- 854 Quartly, G. D. (1998). Determination of oceanic rain rate and rain cell structure from
855 altimeter waveform data. Part I: Theory. *Journal of Atmospheric and Oceanic Tech-*
856 *nology*, 15, 1361–1378.
- 857 Quartly, G. D. (2009). Optimizing σ^0 information from the Jason-2 altimeter. *IEEE*
858 *Geoscience and Remote Sensing Letters*, 6, 398–402.
- 859 Quartly, G. D. (2010). Hyperbolic retracker: removing bright target artefacts from al-
860 timetric waveform data. In *ESA SP-686, Living Planet Symposium 2010, Bergen,*
861 *Norway, (28 June - 2 July 2007)* ESA Publication, SP-686. Noordwijkerhout, NL:
862 ESA.
- 863 Quartly, G. D., Srokosz, M. A., & McMillan, A. C. (2001). Analyzing altimeter arti-
864 facts: Statistical properties of ocean waveforms. *Journal of Atmospheric and Oceanic*
865 *Technology*, 18, 2074–2091.
- 866 Querin, S., Crise, A., Deponte, D., & Solidoro, C. (2006). Numerical study of the role of
867 wind forcing and freshwater buoyancy input on the circulation in a shallow embayment
868 (Gulf of Trieste, Northern Adriatic Sea). *Journal of Geophysical Research: Oceans*
869 *(1978–2012)*, 111.
- 870 Roblou, L., Lamouroux, J., Bouffard, J., Lyard, F., Le Hénaff, M., Lombard, A.,
871 Marsaleix, P., De Mey, P., Birol, F., Vignudelli, S. et al. (2011). Post-processing
872 altimeter data toward coastal applications and integration into coastal models. In
873 S. Vignudelli, A. Kostianoy, P. Cipollini, & J. Benveniste (Eds.), *Coastal Altimetry*
874 (pp. 217–246). Berlin Heidelberg: Springer-Verlag.
- 875 Roblou, L., Lyard, F., Le Henaff, M., & Maraldi, C. (2007). X-TRACK, a new pro-
876 cessing tool for altimetry in coastal oceans. In *IEEE Geoscience and Remote Sensing*
877 *Symposium, Barcelona, Spain, (23-27 July 2007)* (pp. 5129–5133). IEEE.
- 878 Ryan, J., Fischer, A., Kudela, R., McManus, M., Myers, J., Paduan, J., Ruhsam, C.,
879 Woodson, C., & Zhang, Y. (2010). Recurrent frontal slicks of a coastal ocean upwelling
880 shadow. *Journal of Geophysical Research: Oceans (1978–2012)*, 115.
- 881 Schumann, E. H. (1992). Interannual wind variability on the south and east coasts of

882 South Africa. *Journal of Geophysical Research: Atmospheres (1984–2012)*, *97*, 20397–
883 20403.

884 Scozzari, A., Gomez-Enri, J., Vignudelli, S., & Soldovieri, F. (2012). Understanding
885 target-like signals in coastal altimetry: Experimentation of a tomographic imaging
886 technique. *Geophysical Research Letters*, *39*.

887 Soussi, B., & Femenias, P. (2006). ENVISAT RA-2/MWR Level 2 User Manual. *ESA*
888 *User Manual, ESA*, .

889 South African Navy (2007). South African tide tables. *Tokai, South Africa*, .

890 Stravisi, F. (1977). Bora driven circulation in Northern Adriatic. *Bollettino di Geofisica*,
891 *19*, 73–74.

892 Stravisi, F., & Purga, N. (2005). *Il livello del mare a Trieste: piani di riferimento e*
893 *statistiche*. Technical Report 112 Universita' di Trieste, Dipartimento di Scienze della
894 Terra.

895 Thibaut, P., Poisson, J., Bronner, E., & Picot, N. (2010). Relative performance of
896 the MLE3 and MLE4 retracking algorithms on Jason-2 altimeter waveforms. *Marine*
897 *Geodesy*, *33*, 317–335.

898 Tournadre, J. (2007). Signature of lighthouses, ships, and small islands in altimeter
899 waveforms. *Journal of Atmospheric and Oceanic Technology*, *24*, 1143–1149.

900 Tournadre, J., Girard-Ardhuin, F., & Legrésy, B. (2012). Antarctic icebergs distributions,
901 2002–2010. *Journal of Geophysical Research: Oceans (1978–2012)*, *117*.

902 Walsh, E. J. (1982). Pulse-to-pulse correlation in satellite radar altimeters. *Radio Science*,
903 *17*, 786–800.

904 Wingham, D. J. (1988). Onboard correction of mispointing errors in satellite altimeter
905 returns. *IEEE Journal of Oceanic Engineering*, *13*, 77–81.

906 Yang, L., Lin, M., Liu, Q., & Pan, D. (2012). A coastal altimetry retracking strategy
907 based on waveform classification and sub-waveform extraction. *International Journal*
908 *of Remote Sensing*, *33*, 7806–7819.

- 909 Yang, Y., Hwang, C., Hsu, H., Dongchen, E., & Wang, H. (2011). A subwaveform thresh-
910 old retracker for ERS-1 altimetry: A case study in the Antarctic Ocean. *Computers*
911 *and Geosciences*, *41*, 88–98.
- 912 Zanife, O., Vincent, P., Amarouche, L., Dumont, J., Thibaut, P., & Labroue, S. (2003).
913 Comparison of the Ku-band range noise level and the relative sea-state bias of the
914 Jason-1, TOPEX, and Poseidon-1 radar altimeters special issue: Jason-1 calibration/-
915 validation. *Marine Geodesy*, *26*, 201–238.

916 **List of Figures**

917	1	Characteristics of an idealised open ocean waveform.	35
918	2	Radargrams of Envisat track 416 over the Adriatic Sea (cycles 65 to 70). Land is shaded in grey. Every vertical line corresponds to a waveform at a 919 latitude specified on the X axis. Y axis: gate numbers for each waveforms. 920 The colorbar shows the power level for each gate.	36
921	3	The areas of study and the extent of the retracked altimetry passes. Top: 922 Northern Adriatic and Gulf of Trieste. Bottom: Mossel Bay, along the 923 South African coast. Bathymetry is shown by means of contour lines: 924 they are drawn every 10 m.	37
925	4	Flow diagram of ALES retracking procedure for each waveform. Startgate 926 and stopgate refer to the starting gate number and end gate number of the 927 sub-waveform window.	38
928	5	Montecarlo simulation (500 waveforms x gate x SWH value) using Envisat 929 parameters. From upper left to lower right: RMSE difference between 930 Brown full-waveform and subwaveform retracking at different SWH for A) 931 Epoch, B) SWH and C) amplitude estimation; D) relationship between 932 SWH and number of gates needed to estimate the Epoch with a 1 cm 933 tolerance w.r.t. the full sub-waveform retracker. In A) the 1 cm tolerance 934 is specified by a black horizontal line.	39
935	6	Examples of ALES retracking of Jason 2 waveforms for open ocean with 936 SWH=0.75 m (left), coastal ocean with corrupted trailing edge and SWH=1.65 937 m (centre), open ocean with SWH=9.48 m (right).	40
938	7	North Adriatic: percentage of cycles highly correlated with TG time series 939 (correlation coefficient ≥ 0.9) for Env 416 (top), J-1 161 (centre) and J-2 940 196 (bottom). On the x axis the along-track latitude of the nominal tracks 941 are shown. Land is shaded in gray. The distance up to 20 km from the 942 closest coastline is specified by a green line which refers to the y-axis on 943 the right. For J-2 196, the latitude of the islet which separates the gulf 944 from the lagoon is represented by a vertical dashed line.	41
945	8	South Africa: percentage of cycles highly correlated with TG time series 946 (correlation coefficient ≥ 0.9) for Env 687 (top), and J-2 198 (bottom). On 947 the x axis the along-track latitude of the nominal tracks are shown. Land 948 is shaded in gray. The distance up to 20 km from the closest coastline is 949 specified by a green line which refers to the y-axis on the right.	42
950	9	North Adriatic: percentage of outliers for Env 416 (top), J-1 161 (centre) 951 and J-2 196 (bottom). On the x axis the along-track latitude of the nominal 952 tracks is shown. Land is shaded in gray. The distance up to 20 km from 953 the closest coastline is specified by a green line which refers to the y-axis 954 on the right. For J-2 196, the latitude of the islet which separates the gulf 955 from the lagoon is represented by a vertical dashed line.	43
956	10	South Africa: percentage of outliers for Env 687 (top), and J-2 198 (bot- 957 tom). On the x axis the along-track latitude of the nominal tracks is 958 shown. Land is shaded in gray. The distance up to 20 km from the closest 959 coastline is specified by a green line which refers to the y-axis on the right.	44
960			

961	11	North Adriatic: correlation coefficient between Trieste TG and Env 416	
962		(top), J-1 161 (centre) and J-2 196 (bottom). On the x axis the along-	
963		track latitude of the nominal tracks is shown and the latitude of the TG	
964		is highlighted with a black dot. Land is shaded in gray. The distance up	
965		to 20 km from the closest coastline is specified by a green line which refers	
966		to the y-axis on the right. For J-2 196, the latitude of the islet which	
967		separates the gulf from the lagoon is represented by a vertical dashed line.	
968		Negative values and correlation computed for less than 10 points in the	
969		time series are not shown.	45
970	12	South Africa: correlation coefficient between Mossel Bay TG and Env 687	
971		(top), and J-2 198 (bottom). On the x axis the along-track latitude of the	
972		nominal tracks is shown and the latitude of the TG is highlighted with a	
973		black dot. Land is shaded in gray. The distance up to 20 km from the	
974		closest coastline is specified by a green line which refers to the y-axis on	
975		the right. Negative values and correlation computed for less than 10 points	
976		in the time series are not shown.	46
977	13	North Adriatic: absolute RMS difference between Trieste TG and Env 416	
978		(top), J-1 161 (centre) and J-2 196 (bottom). On the x axis the along-track	
979		latitude of the nominal tracks is shown. Black dots on the x axis highlight	
980		the latitude of the TG (big dot) and of the closest point along track (small	
981		dot). Land is shaded in gray. The distance up to 20 km from the closest	
982		coastline is specified by a green line which refers to the y-axis on the right.	
983		A black dashed line marks the difference between the along track mean	
984		sea surface (DTU10) and the mean sea surface DTU10 at the TG. For J-2	
985		196, the latitude of the islet which separates the gulf from the lagoon is	
986		represented by a vertical dashed line and	47
987	14	South Africa: RMS of the difference between Mossel Bay TG values and	
988		Env 687 TWLE (top), and J-2 198 TWLE (bottom). The mean of the	
989		difference for each along track location was removed. On the x axis the	
990		along-track latitude of the nominal tracks is shown. Black dots on the x	
991		axis highlight the latitude of the TG (big dot) and of the closest point	
992		along track (small dot). Land is shaded in gray. The distance up to 20 km	
993		from the closest coastline is specified by a green line which refers to the	
994		y-axis on the right.	48
995	15	Histograms of consecutive TWLE differences in modulus for each track for	
996		SGDR (blue) and ALES (red). Coloumns of SGDR are thinner in order	
997		to facilitate the distinction.	49

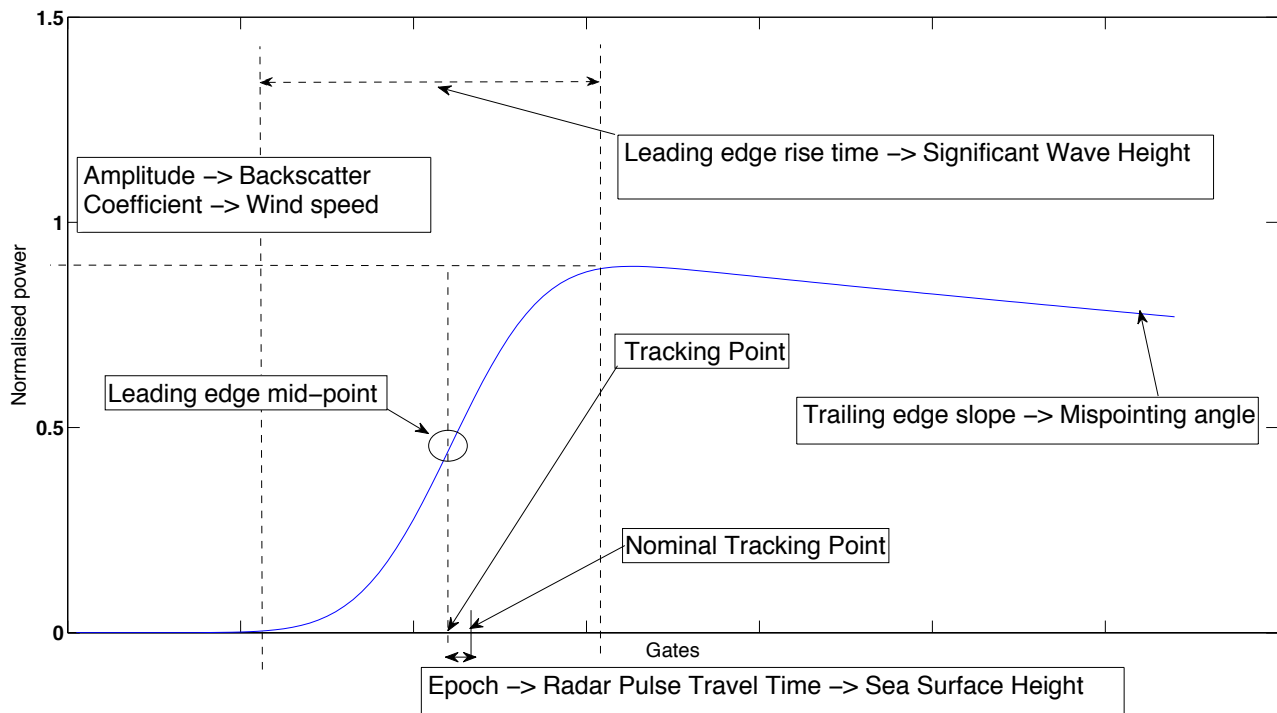


Figure 1: Characteristics of an idealised open ocean waveform.

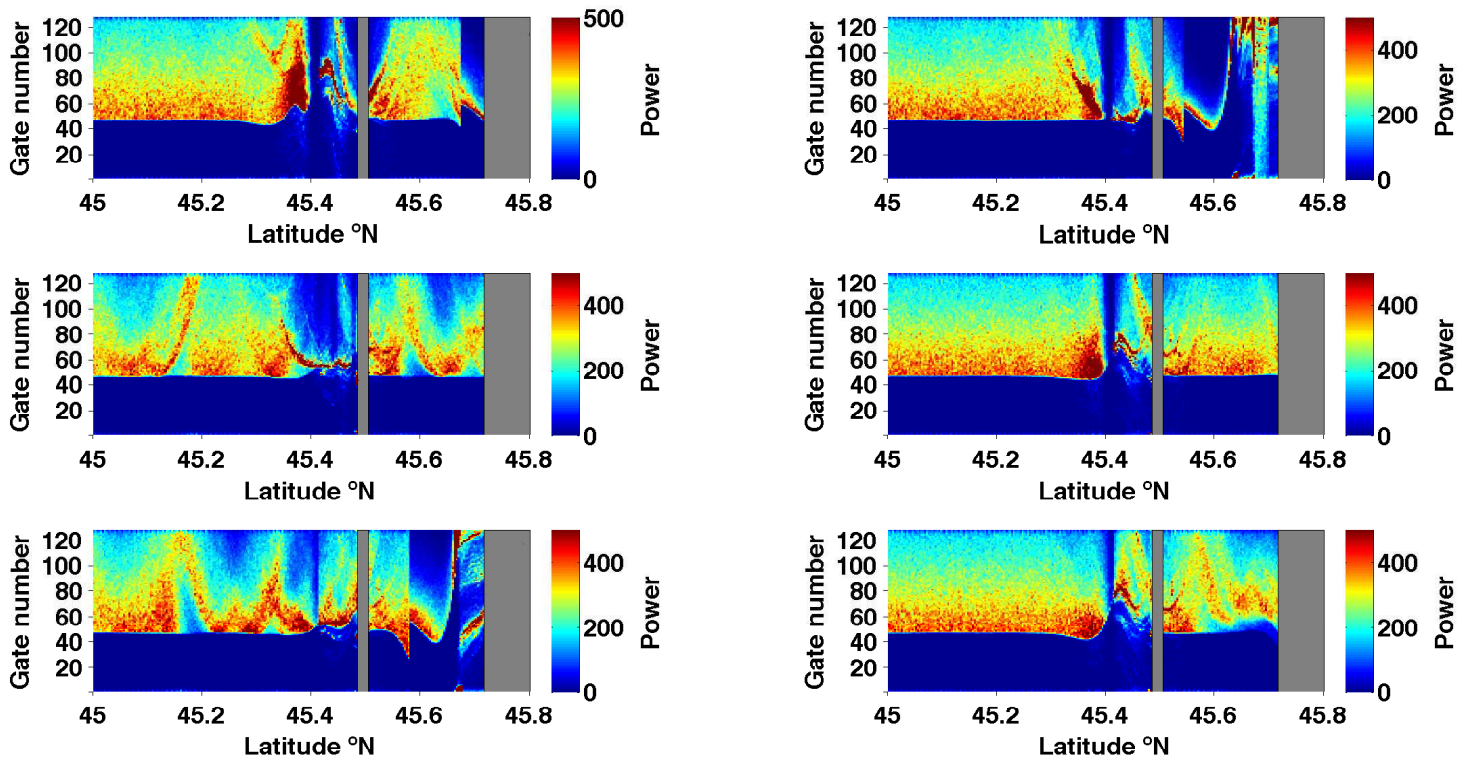


Figure 2: Radargrams of Envisat track 416 over the Adriatic Sea (cycles 65 to 70). Land is shaded in grey. Every vertical line corresponds to a waveform at a latitude specified on the X axis. Y axis: gate numbers for each waveforms. The colorbar shows the power level for each gate.

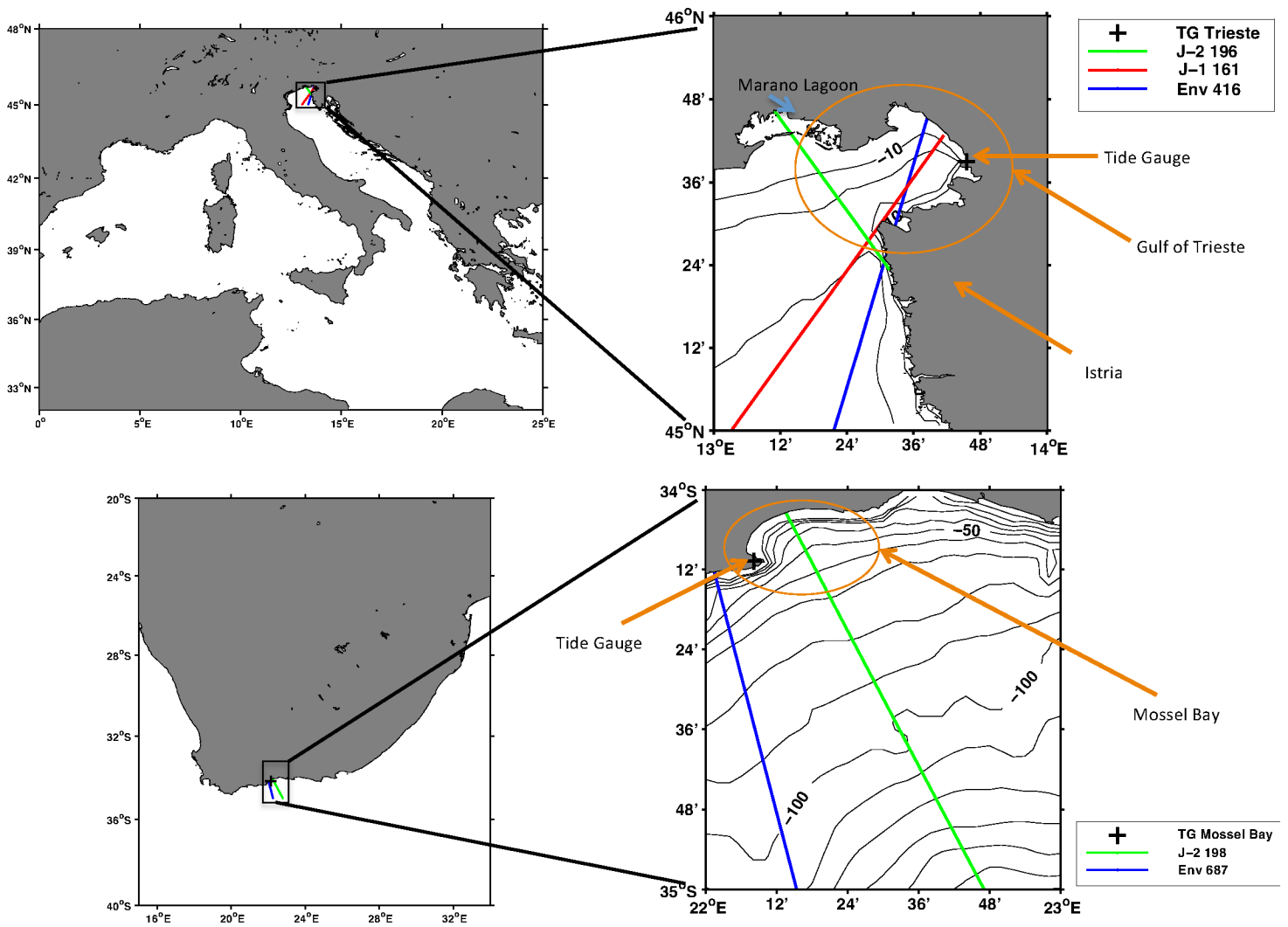


Figure 3: The areas of study and the extent of the retracked altimetry passes. Top: Northern Adriatic and Gulf of Trieste. Bottom: Mossel Bay, along the South African coast. Bathymetry is shown by means of contour lines: they are drawn every 10 m.

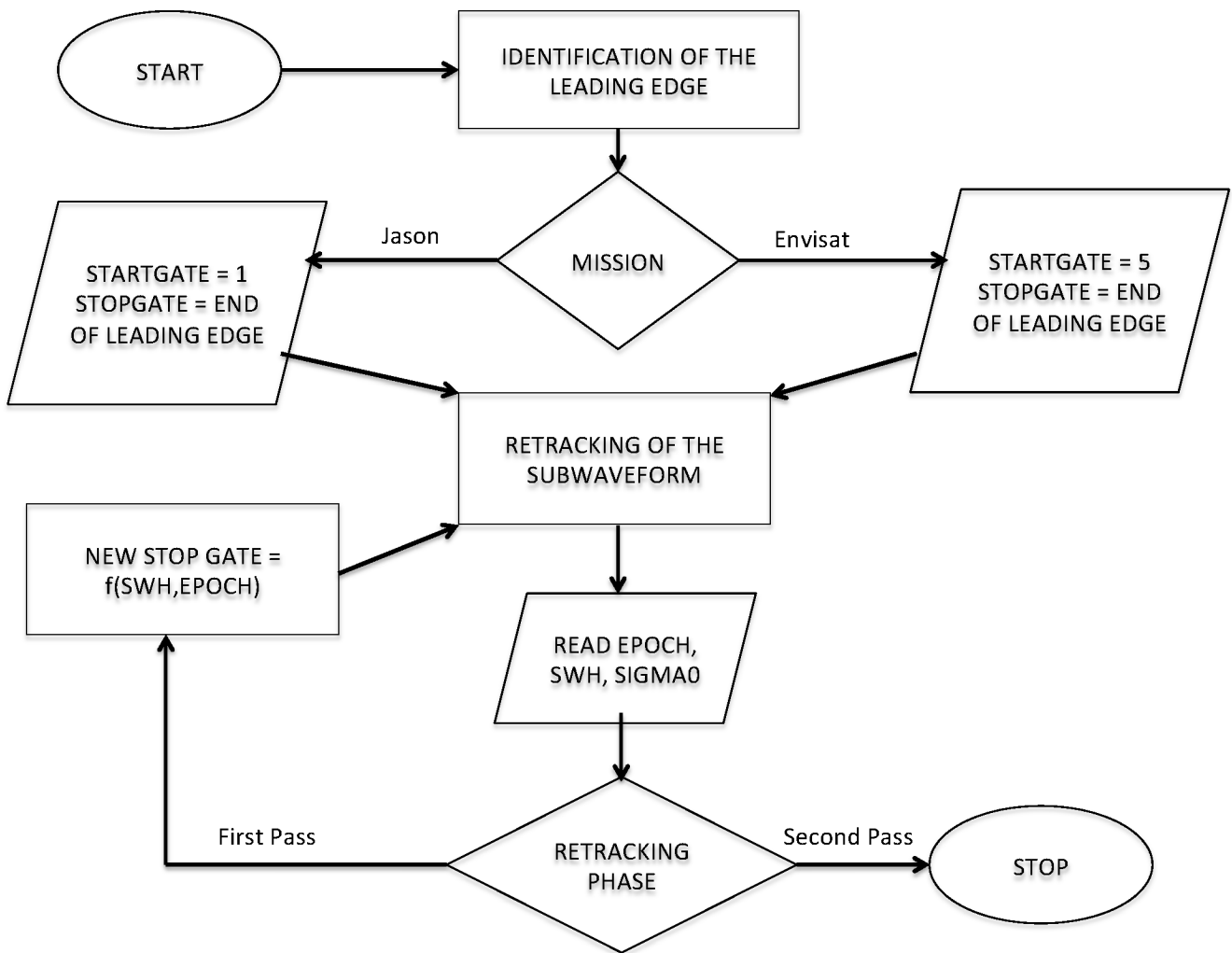


Figure 4: Flow diagram of ALES retracking procedure for each waveform. Startgate and stopgate refer to the starting gate number and end gate number of the sub-waveform window.

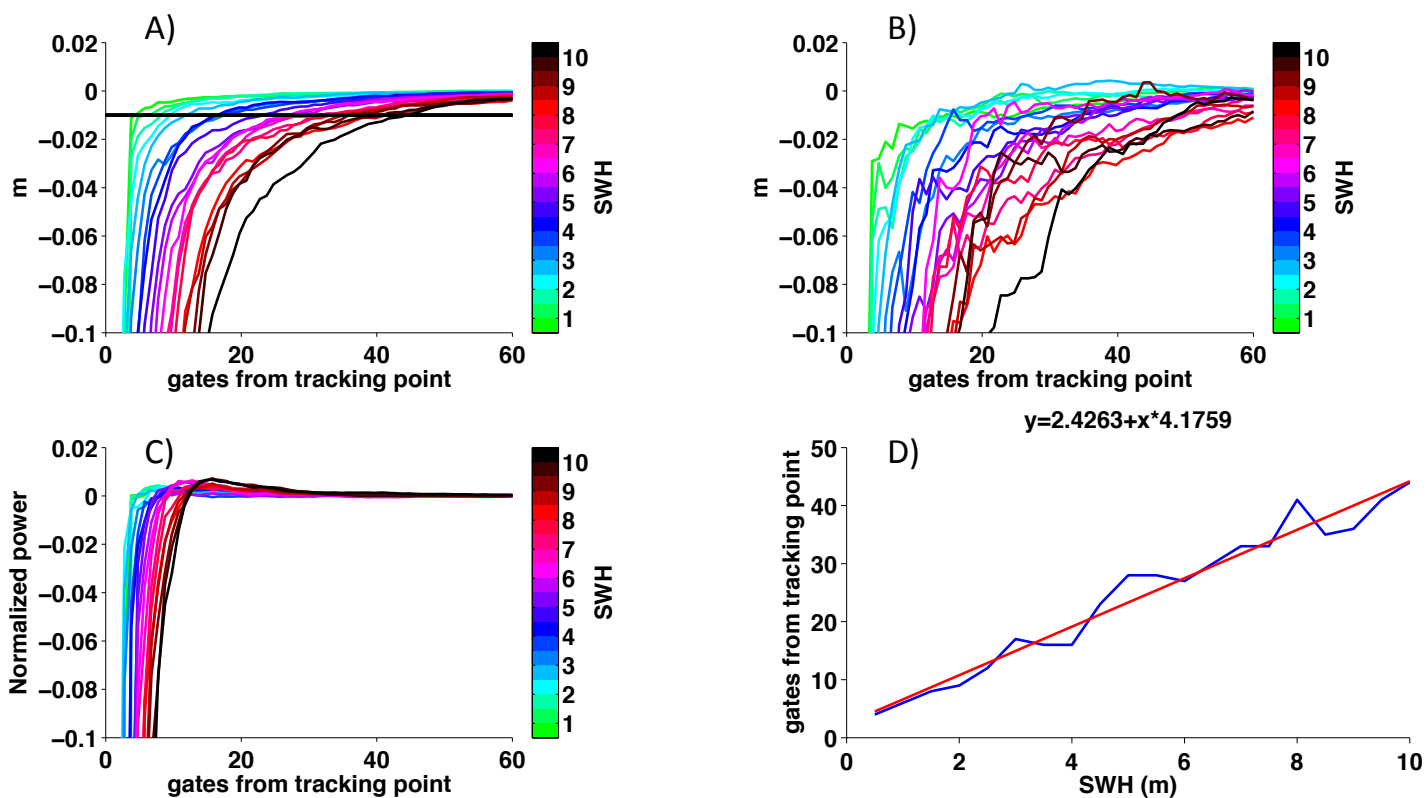


Figure 5: Montecarlo simulation (500 waveforms x gate x SWH value) using Envisat parameters. From upper left to lower right: RMSE difference between Brown full-waveform and subwaveform retracking at different SWH for A) Epoch, B) SWH and C) amplitude estimation; D) relationship between SWH and number of gates needed to estimate the Epoch with a 1 cm tolerance w.r.t. the full sub-waveform retracker. In A) the 1 cm tolerance is specified by a black horizontal line.

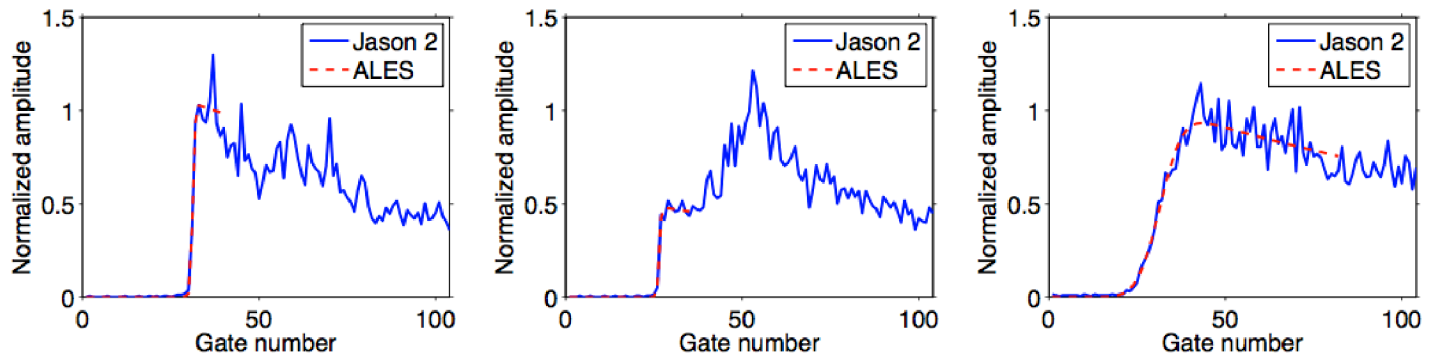


Figure 6: Examples of ALES retracking of Jason 2 waveforms for open ocean with SWH=0.75 m (left), coastal ocean with corrupted trailing edge and SWH=1.65 m (centre), open ocean with SWH=9.48 m (right).

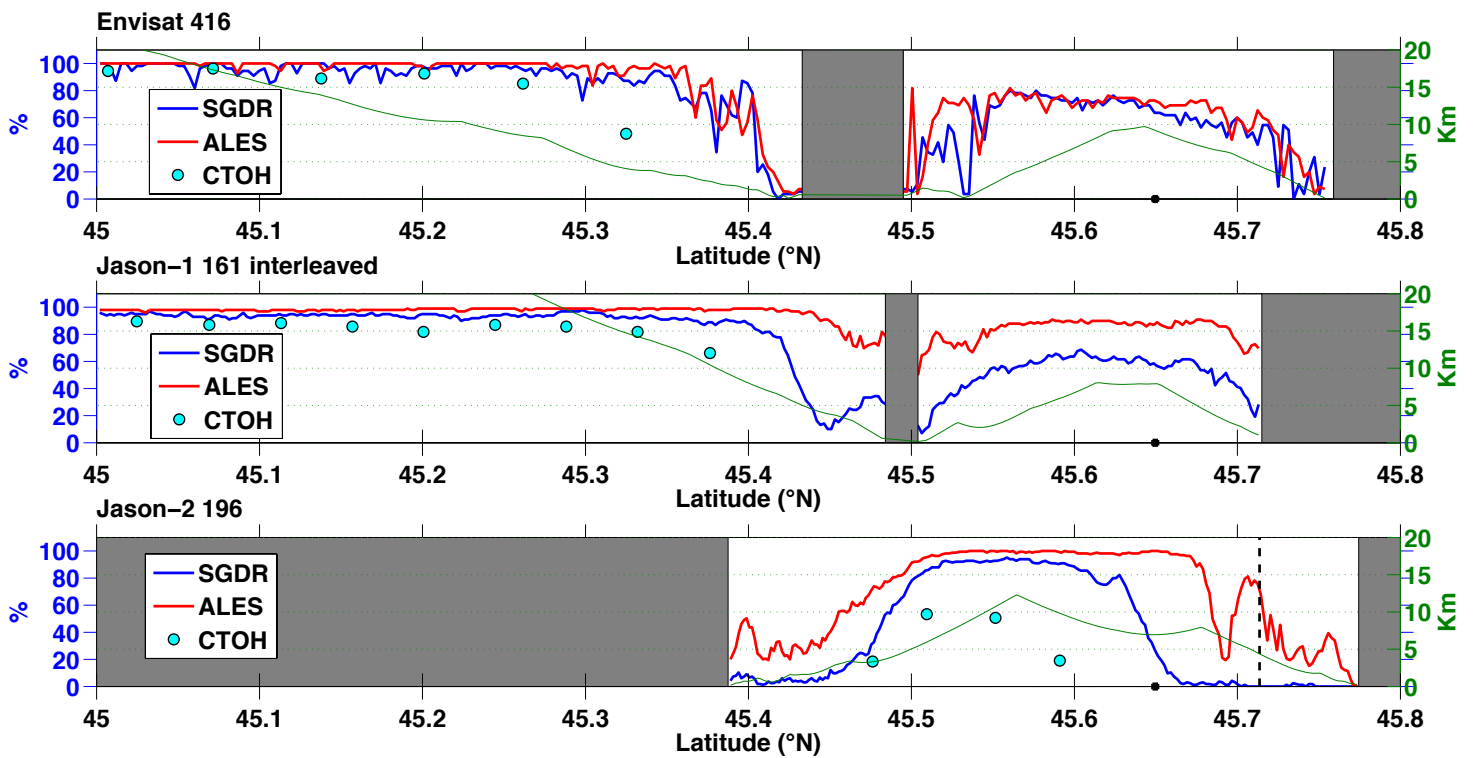


Figure 7: North Adriatic: percentage of cycles highly correlated with TG time series (correlation coefficient ≥ 0.9) for Env 416 (top), J-1 161 (centre) and J-2 196 (bottom). On the x axis the along-track latitude of the nominal tracks are shown. Land is shaded in gray. The distance up to 20 km from the closest coastline is specified by a green line which refers to the y-axis on the right. For J-2 196, the latitude of the islet which separates the gulf from the lagoon is represented by a vertical dashed line.

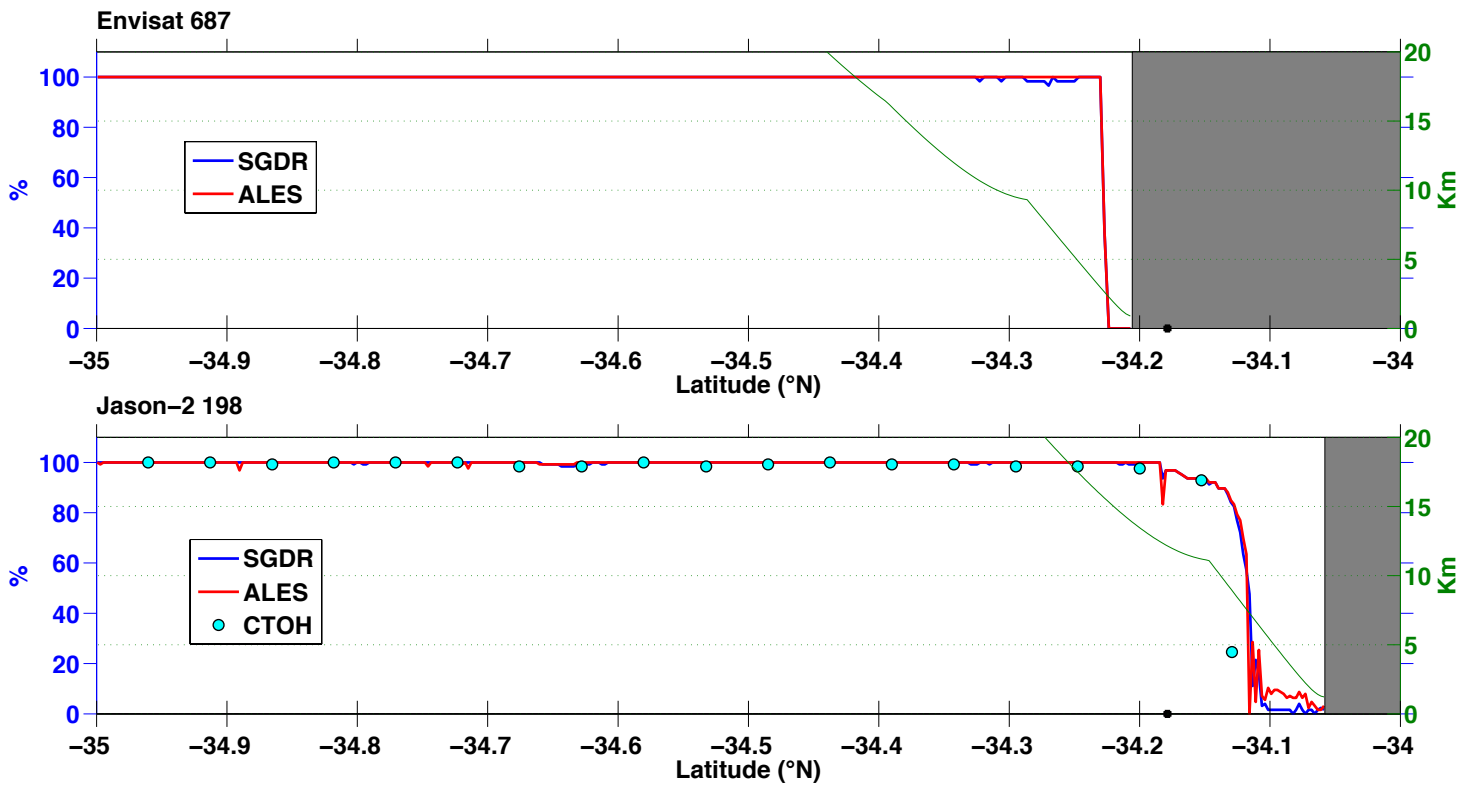


Figure 8: South Africa: percentage of cycles highly correlated with TG time series (correlation coefficient ≥ 0.9) for Env 687 (top), and J-2 198 (bottom). On the x axis the along-track latitude of the nominal tracks are shown. Land is shaded in gray. The distance up to 20 km from the closest coastline is specified by a green line which refers to the y-axis on the right.

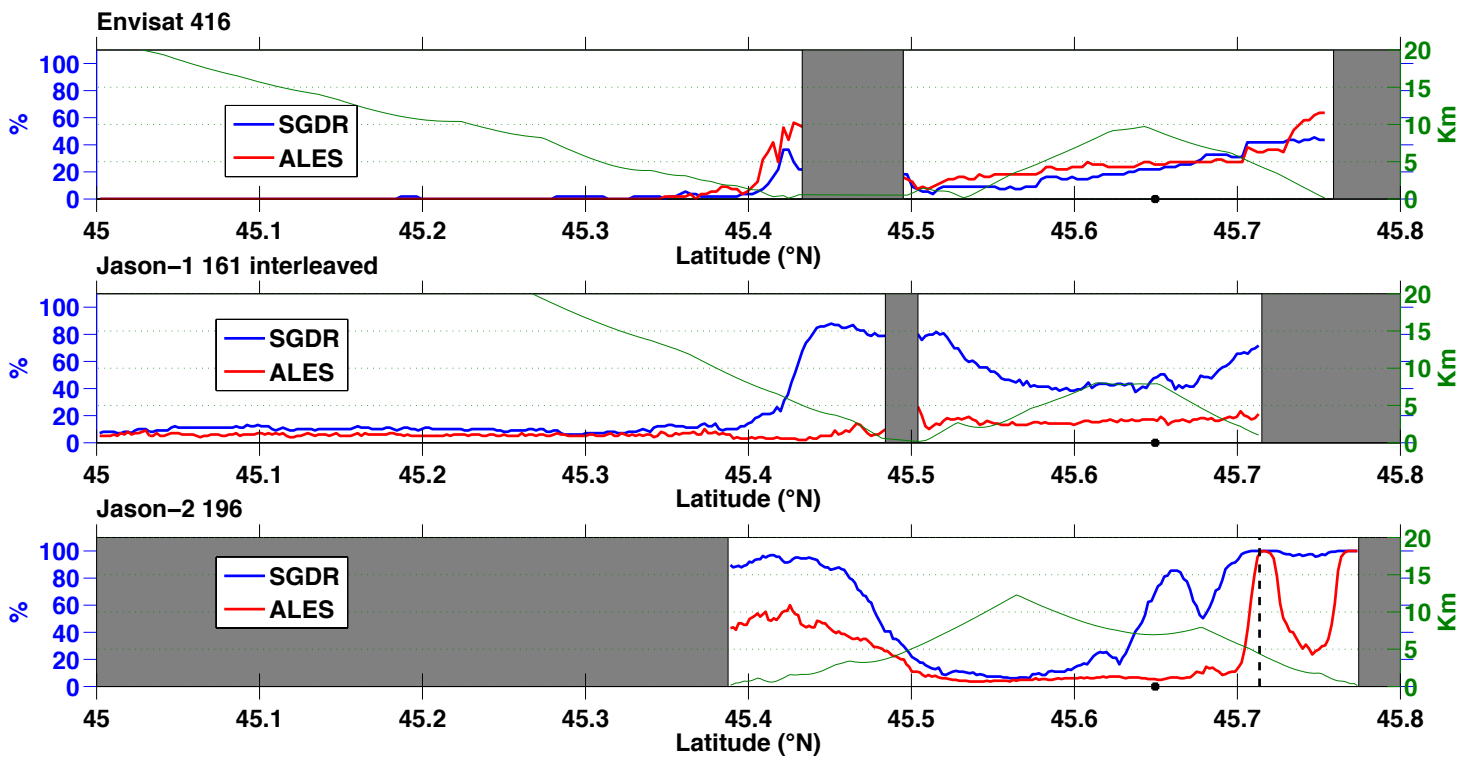


Figure 9: North Adriatic: percentage of outliers for Env 416 (top), J-1 161 (centre) and J-2 196 (bottom). On the x axis the along-track latitude of the nominal tracks is shown. Land is shaded in gray. The distance up to 20 km from the closest coastline is specified by a green line which refers to the y-axis on the right. For J-2 196, the latitude of the islet which separates the gulf from the lagoon is represented by a vertical dashed line.

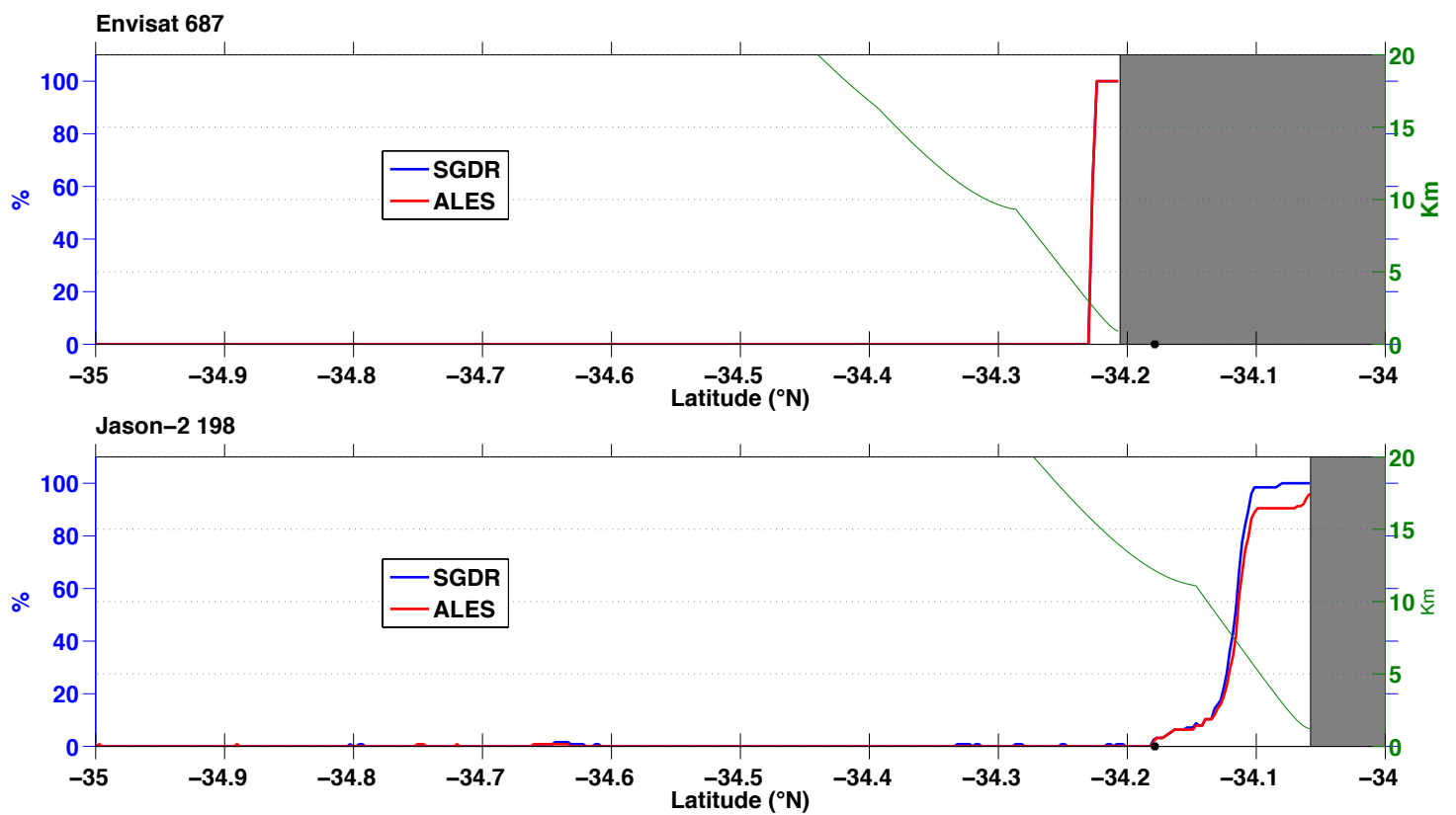


Figure 10: South Africa: percentage of outliers for Env 687 (top), and J-2 198 (bottom). On the x axis the along-track latitude of the nominal tracks is shown. Land is shaded in gray. The distance up to 20 km from the closest coastline is specified by a green line which refers to the y-axis on the right.

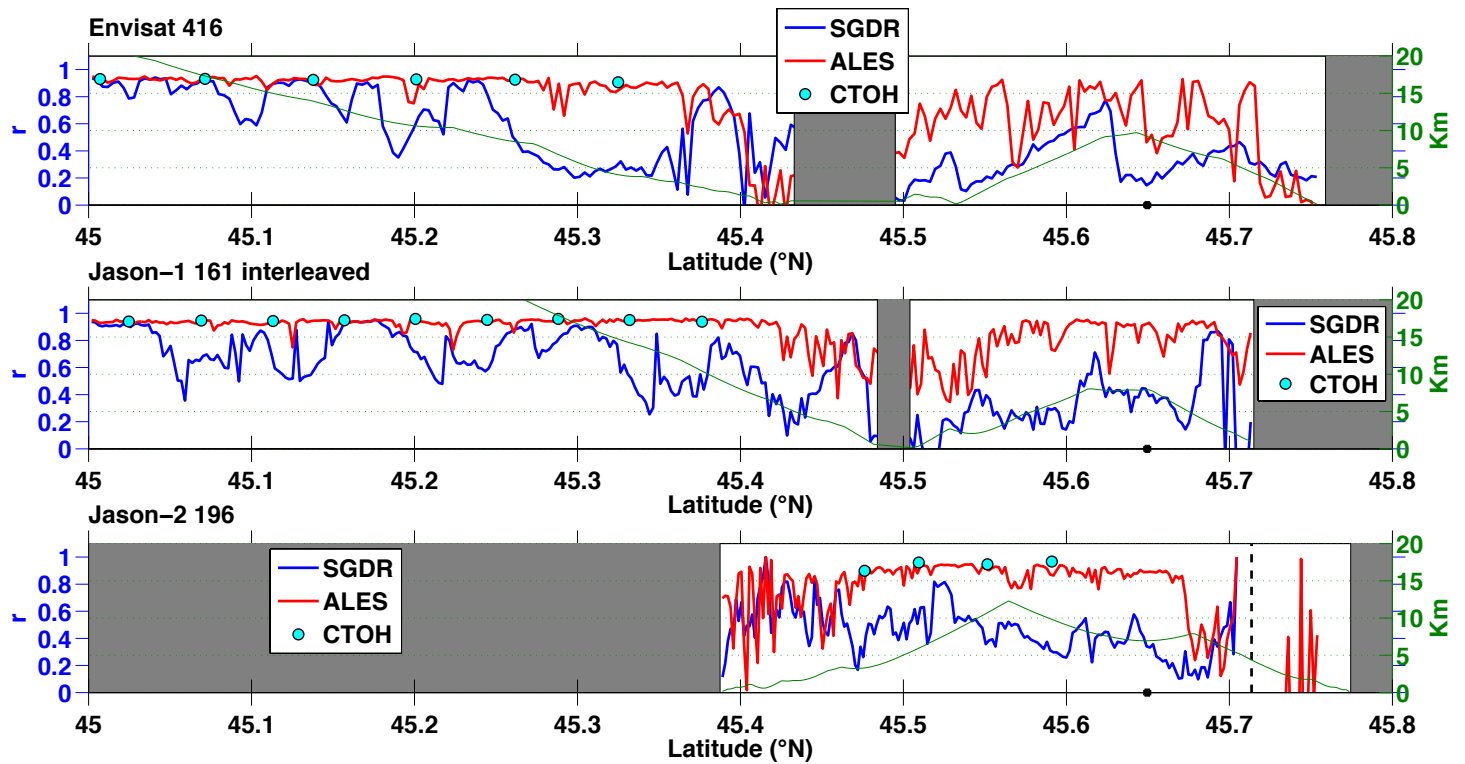


Figure 11: North Adriatic: correlation coefficient between Trieste TG and Env 416 (top), J-1 161 (centre) and J-2 196 (bottom). On the x axis the along-track latitude of the nominal tracks is shown and the latitude of the TG is highlighted with a black dot. Land is shaded in gray. The distance up to 20 km from the closest coastline is specified by a green line which refers to the y-axis on the right. For J-2 196, the latitude of the islet which separates the gulf from the lagoon is represented by a vertical dashed line. Negative values and correlation computed for less than 10 points in the time series are not shown.

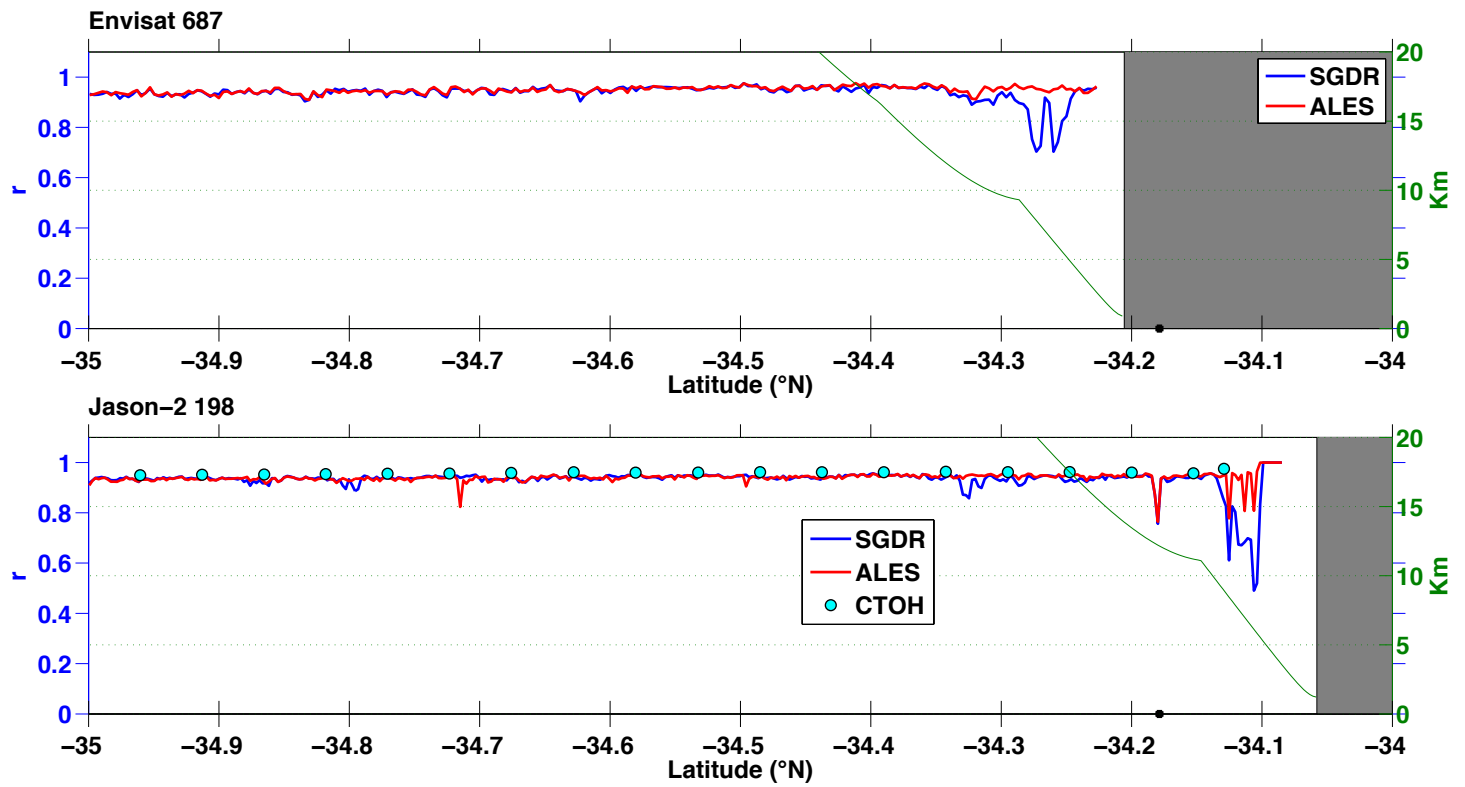


Figure 12: South Africa: correlation coefficient between Mossel Bay TG and Env 687 (top), and J-2 198 (bottom). On the x axis the along-track latitude of the nominal tracks is shown and the latitude of the TG is highlighted with a black dot. Land is shaded in gray. The distance up to 20 km from the closest coastline is specified by a green line which refers to the y-axis on the right. Negative values and correlation computed for less than 10 points in the time series are not shown.

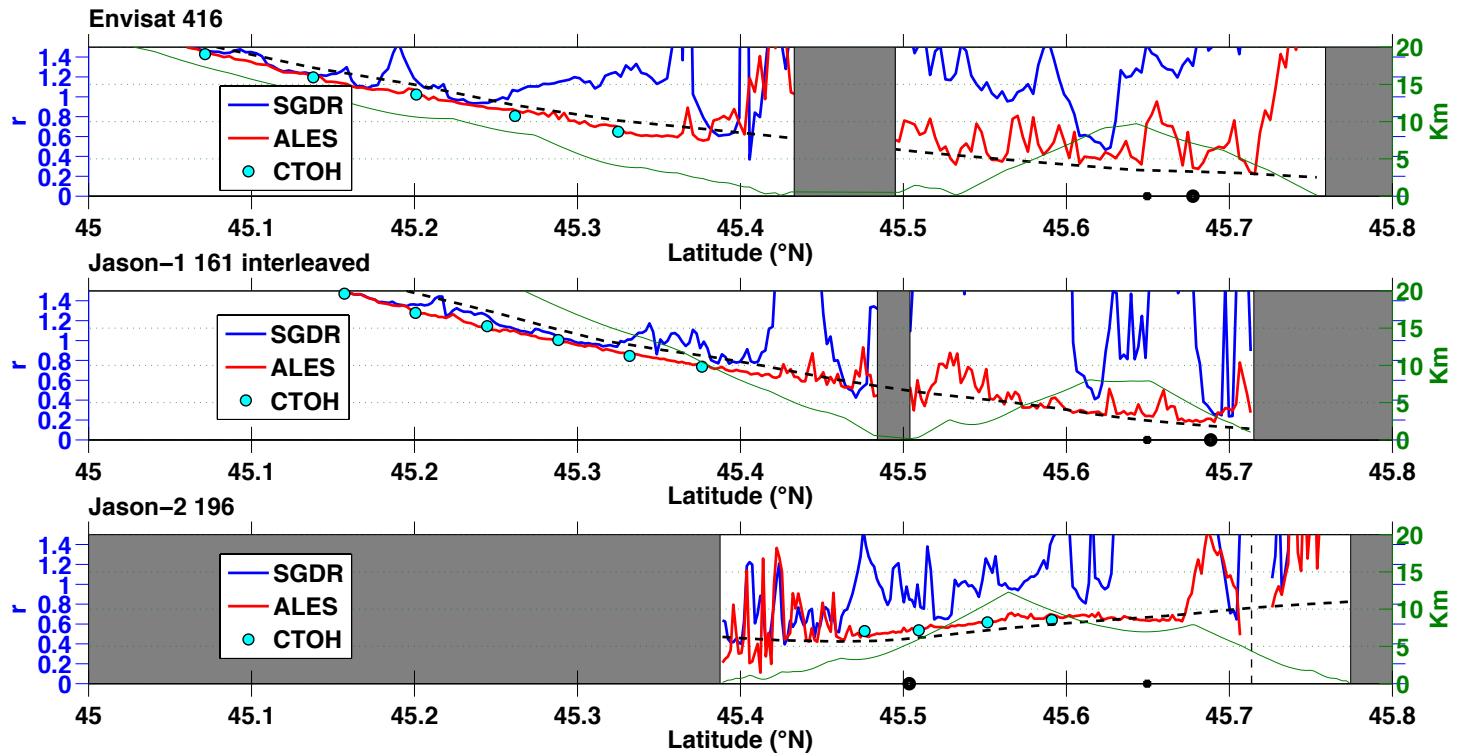


Figure 13: North Adriatic: absolute RMS difference between Trieste TG and Env 416 (top), J-1 161 (centre) and J-2 196 (bottom). On the x axis the along-track latitude of the nominal tracks is shown. Black dots on the x axis highlight the latitude of the TG (big dot) and of the closest point along track (small dot). Land is shaded in gray. The distance up to 20 km from the closest coastline is specified by a green line which refers to the y-axis on the right. A black dashed line marks the difference between the along track mean sea surface (DTU10) and the mean sea surface DTU10 at the TG. For J-2 196, the latitude of the islet which separates the gulf from the lagoon is represented by a vertical dashed line and

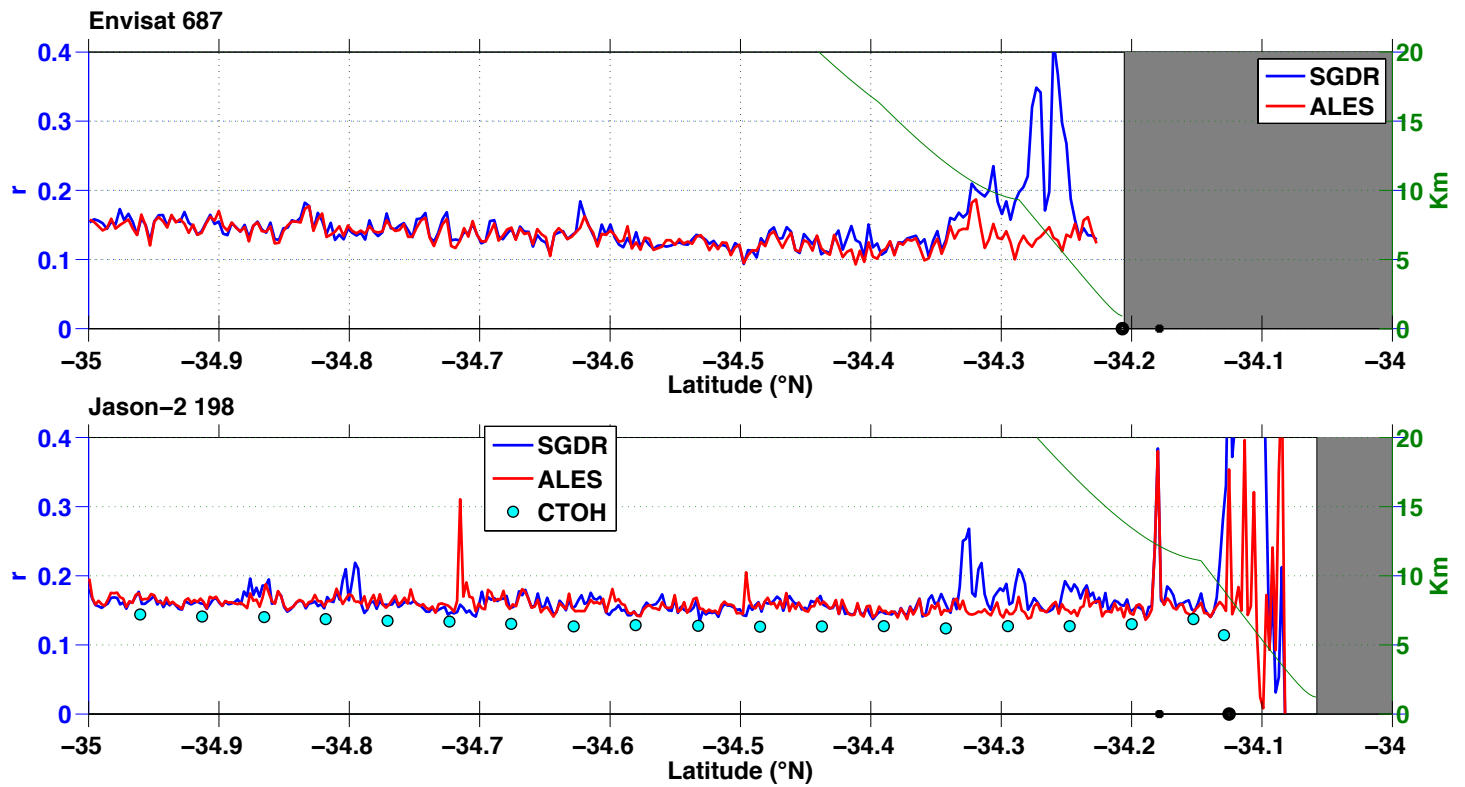


Figure 14: South Africa: RMS of the difference between Mossel Bay TG values and Env 687 TWLE (top), and J-2 198 TWLE (bottom). The mean of the difference for each along track location was removed. On the x axis the along-track latitude of the nominal tracks is shown. Black dots on the x axis highlight the latitude of the TG (big dot) and of the closest point along track (small dot). Land is shaded in gray. The distance up to 20 km from the closest coastline is specified by a green line which refers to the y-axis on the right.

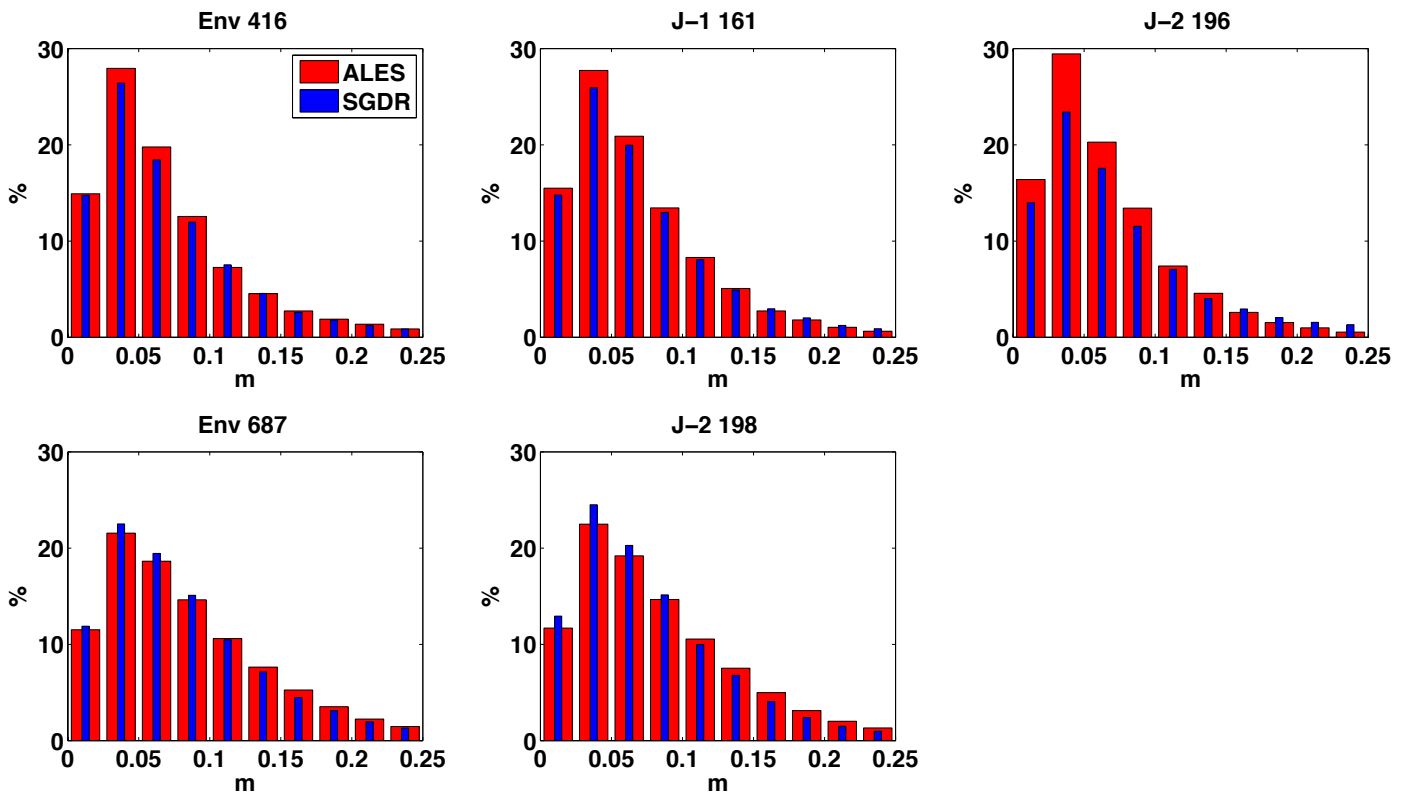


Figure 15: Histograms of consecutive TWLE differences in modulus for each track for SGDR (blue) and ALES (red). Columns of SGDR are thinner in order to facilitate the distinction.

998 **List of Tables**

999	1	Data availability for this study. Row 2: the tide gauge to which the tracks specified in each column are compared. Row 3: Minimum distance between the tide gauge and the closest point on each satellite track. Row 4: number of reprocessed SGDR cycles; all the cycles where data in the area were available have been taken into account; the number refers to the number of cycles during which tide gauge data were also available. Row 5: number of CTOH cycles available. Row 6: number and percentage of 18 Hz (20 Hz) along track points where no waveforms from the SGDR of Envisat (Jason) were available. For Envisat, this also includes cases where waveforms were present, but the bandwidth in use was not 320 MHz. Row 7: number and percentage of along track points where no estimation of altimetric parameters was available in the SGDR, despite the availability of corresponding waveforms.	51
1000			
1001			
1002			
1003			
1004			
1005			
1006			
1007			
1008			
1009			
1010			
1011			
1012	2	List of cycles. Column 2: list of the cycles used in this study for each satellite track. Cycles where satellite data were missing and/or coincident tide gauge data were not available have been excluded. The square brackets indicate the range of cycles including the extremes. Column 3: time interval in day/month/year format.	52
1013			
1014			
1015			
1016			
1017	3	Validation results. Row 2: Outliers in absolute number and percentage of the total number of available waveforms. Row 3: median of the correlation of TWLE for each track with the correspondent tide gauge heights. Row 4 (rel): median value of the along-track relative RMS of the difference between TWLE and TG sea level height anomaly, with mean of the difference removed. Row 4 (abs): RMS of the difference of the absolute sea level heights above the ellipsoid at the closest point between TG and satellite tracks.	53
1018			
1019			
1020			
1021			
1022			
1023			
1024			
1025	4	Criteria for valid points: minimum and maximum values of TWLE, SWH and σ^0	54
1026			
1027	5	Mean, standard deviation and percentiles (1st and 99th) of TWLE distributions for ALES (outliers removed) compared with SGDR. The total number of valid sea level observations for each track is reported in the last row.	55
1028			
1029			
1030			
1031	6	Mean biases with standard deviation between SGDR and ALES TWLE estimations. Biases were computed using only along-track points where correlation coefficient with TG was higher than 0.9 and more than 50% of valid points were available for both SGDR and ALES. No such points were found for J-2 196, whose bias is therefore not computed.	56
1032			
1033			
1034			
1035			

Table 1: Data availability for this study. Row 2: the tide gauge to which the tracks specified in each column are compared. Row 3: Minimum distance between the tide gauge and the closest point on each satellite track. Row 4: number of reprocessed SGDR cycles; all the cycles where data in the area were available have been taken into account; the number refers to the number of cycles during which tide gauge data were also available. Row 5: number of CTOH cycles available. Row 6: number and percentage of 18 Hz (20 Hz) along track points where no waveforms from the SGDR of Envisat (Jason) were available. For Envisat, this also includes cases where waveforms were present, but the bandwidth in use was not 320 MHz. Row 7: number and percentage of along track points where no estimation of altimetric parameters was available in the SGDR, despite the availability of corresponding waveforms.

	Env 416	Env 687	J-1 161	J-2 196	J-2 198
Tide Gauge	Trieste	Mossel Bay	Trieste	Trieste	Mossel Bay
Minimum Distance	11.78 km	10.72 km	8.23 km	30.60 km	13.37 km
Number of SGDR cycles	57	58	99	165	126
Number of CTOH cycles	56	N/A	77	152	126
Missing waveforms	325 (2.71%)	0	1483 (4.77%)	5253 (15.45%)	1267 (2.53%)
Missing SGDR outputs	518 (4.32%)	384 (2.74%)	5966 (19.19%)	17653 (51.94%)	2981 (5.95%)

Table 2: List of cycles. Coloumn 2: list of the cycles used in this study for each satellite track. Cycles where satellite data were missing and/or coincident tide gauge data were not available have been excluded. The square brackets indicate the range of cycles including the extremes. Coloumn 3: time interval in day/month/year format.

	Valid cycles	Time interval
Env 416	10 [12,14] 16 19 27 30 [42,45] 47 [49,52] [54,58] [60,72] [74,93]	15/10/02 - 26/09/10
Env 687	[14,17] [19,21] [23,26] 29 31 32 44 45 [47,50] [52,58] [62,73] [75,93]	13/03/03 - 7/10/10
J-1 161	[262,283] [285,292] [295,303] [306,340] [342,349] [351,363] [366,370]	16/02/09 - 23/01/12
J-2 196	[1,165]	19/07/08 - 31/12/12
J-2 198	[1,8] [12,14] [18,30] [32,35] [37,42] 45 46 [48, 80] 82 83 [85,91] [95,100] [102, 109] [111,132] [138,146]	19/07/08 - 26/06/12

Table 3: Validation results. Row 2: Outliers in absolute number and percentage of the total number of available waveforms. Row 3: median of the correlation of TWLE for each track with the correspondent tide gauge heights. Row 4 (rel): median value of the along-track relative RMS of the difference between TWLE and TG sea level height anomaly, with mean of the difference removed. Row 4 (abs): RMS of the difference of the absolute sea level heights above the ellipsoid at the closest point between TG and satellite tracks.

		Env 416	Env 687	J-1 161	J-2 196	J-2 198
Outliers	SGDR	1131 (9.43%)	384 (2.75%)	8930(28.72%)	20019 (58.90%)	3393 (6.78%)
	ALES	1421 (11.85%)	384 (2.74%)	2763 (8.89%)	9360 (27.54%)	3052 (6.10%)
Correlation	SGDR	0.44	0.95	0.60	0.44	0.94
	ALES	0.88	0.95	0.93	0.87	0.94
RMS	SGDR	1.31 m (abs)	0.14 m (rel)	0.30 m (abs)	0.85 m (abs)	0.16 m (rel)
	ALES	0.29 m (abs)	0.14 m (rel)	0.21 m (abs)	0.53 m (abs)	0.16 m (rel)

Table 4: Criteria for valid points: minimum and maximum values of TWLE, SWH and σ^0 .

	Min	Max
TWLE (m)	- 2 - min TG value	+ 2 + max TG value
SWH (m)	0	11
σ^0 (dB)	7	30

Table 5: Mean, standard deviation and percentiles (1st and 99th) of TWLE distributions for ALES (outliers removed) compared with SGDR. The total number of valid sea level observations for each track is reported in the last row.

		Env 416	Env 687	J-1 161	J-2 196	J-2 198
Mean	SGDR	0.3 cm	0.1 cm	-0.4 cm	-2.2 cm	0.0 cm
	ALES	-0.4 cm	0.0 cm	-0.1 cm	-0.2 cm	0.1 cm
StD	SGDR	38.5 cm	10.1 cm	31.9 cm	47.6 cm	9.7 cm
	ALES	31.4 cm	10.1 cm	15.6 cm	17.5 cm	10.5 cm
1% - 99%	SGDR	[-108.0 +94.7] cm	[-25.3 +25.5] cm	[-78.9 +70.5] cm	[-1.8 +99.8] cm	[-22.4 +22.1] cm
	ALES	[-93.5 +77.9] cm	[-26.1 +26.1] cm	[-28.8 +29.4] cm	[-34.5 +28.5] cm	[-25.00 +25.2] cm
Obs Num		10569	13594	24394	15721	46662

Table 6: Mean biases with standard deviation between SGDR and ALES TWLE estimations. Biases were computed using only along-track points where correlation coefficient with TG was higher than 0.9 and more than 50% of valid points were available for both SGDR and ALES. No such points were found for J-2 196, whose bias is therefore not computed.

	Env 416	Env 687	J-1 161	J-2 198
Bias TWLE (cm)	-1.3 \pm 3.5	-1.7 \pm 2.6	-1.2 \pm 4.4	-0.3 \pm 3.4